Journal of Volcanology and Geothermal Research 421 (2022) 107430

Contents lists available at ScienceDirect

Journal of Volcanology and Geothermal Research

journal homepage: www.elsevier.com/locate/jvolgeores

Inter- and intra-crystal quartz $\delta^{18}O$ homogeneity at Okataina volcano, Aotearoa New Zealand: Implications for rhyolite genesis

May Sas [a,*], Phil Shane [b], Noriyuki Kawasaki [c], Naoya Sakamoto [d], Georg F. Zellmer [e], Hisayoshi Yurimoto [c,d]

[a] Geology Department, Western Washington University, Bellingham, Washington 98225, USA
[b] School of Environment, University of Auckland, Auckland 1142, New Zealand
[c] Natural History Sciences, Hokkaido University, Sapporo 060-0810, Japan
[d] Isotope Imaging Laboratory, Creative Research Institution, Hokkaido University, Sapporo 001-0021, Japan
[e] Volcanic Risk Solutions, Massey University, Private Bag 11222, Palmerston North 4442, New Zealand

ARTICLE INFO

Article history:
Received 24 June 2021
Received in revised form 11 November 2021
Accepted 16 November 2021
Available online 20 November 2021

Keywords:
Stable isotopes
Caldera
Petrogenesis
Rhyolite
Quartz

ABSTRACT

The sources and processes involved in the genesis of the voluminous rhyolitic magmas of cataclysmic caldera-forming eruptions, and the intervening lower-volume intra-caldera extrusions, have been subject to much debate. To better understand generation of high-volume and low-volume silicic eruptions within a single volcanic centre, and how they may differ, we examined ten volumetrically varied high-SiO_2 rhyolite eruptions from the Okataina Volcanic Centre (OVC) in Aotearoa New Zealand. The OVC is one of the world's most recurrently active silicic volcanoes. In the last ~600 ky, the OVC was the focus of three known caldera-forming events and numerous intermittent dome-building and fissure eruption episodes, with rhyolitic eruption activity as recent as 1314 CE. To elucidate how mass contributions from the mantle and crust may have fluctuated over the lifespan of the OVC magmatic system, oxygen isotopic ratios ($\delta^{18}O$) of quartz in rhyolites were investigated for the first time at inter-crystal and intra-crystal scales. Quartz crystals from four eruption episodes (two caldera-forming events, Utu, ~557 ka, Rotoiti, ~45 ka, and two intra-caldera dome-building events, Rotoma, ~9.5 ka, and Kaharoa, ~0.7 ka) yielded intra-crystal $\delta^{18}O$ isotopic homogeneity ($\pm$0.23‰, 2sd) based on secondary ion mass spectrometry (SIMS). These samples also display inter-crystal and inter-unit homogeneity within slightly lower precision (7.6 $\pm$ 0.5‰, 2sd). Whole-crystal quartz from the same four units, as well as six other units (two intra-caldera dome-building episodes, Okareka, ~21.8 ka, Whakatane, ~5.5 ka, three pre-Rotoiti extra-caldera domes, Round Hill, Haparangi, Kakapiko, and one immediately post-Rotoiti eruption, Earthquake Flat), were then examined using high-precision laser fluorination. Single crystals also yielded mostly homogenous ratios with average $\delta^{18}O$ = 7.6 $\pm$ 0.5‰ (2sd), which is consistent with intra-crystal SIMS analyses, albeit for a larger set of samples. Stable and radiogenic isotope mixing models using the newly obtained $\delta^{18}O$ ratios demonstrate that OVC rhyolites can be produced by ≥25% assimilation of a regional (Torlesse-like) metasedimentary endmember by a depleted mantle source with slightly variable amounts of subduction flux, and that any incorporation of hydrothermally altered material to the system is limited to <5% in caldera and intra-caldera eruptions. The $\delta^{18}O$ records of the OVC are among the most homogenous currently known and indicate stable and consistent mantle and crustal contributions across the lifespan of the magmatic system, with assimilation largely occurring prior to segregation of rhyolitic melts within the silicic reservoir. This isotopic homogeneity may be due to a relatively high-volume and constant magma flux at the OVC, which contrasts to other rhyolitic caldera volcanoes with greater isotopic variability.

1. Introduction

In addition to fractional crystallization, incorporation of crustal mass is thought to be significant in rhyolite genesis, with some studies suggesting as much as 25–30% assimilation of crustal materials (e.g., Long Valley, Bindeman and Valley, 2002; Maroa, McCulloch et al., 1994). These estimates of crustal versus mantle contributions are based on compositional and isotopic models, the latter of which commonly act as evidence for assimilation processes. Major shifts (e.g., >1‰) in oxygen isotopic ratios ($\delta^{18}O$) of rocks and phenocrysts associated with caldera collapse at rhyolite volcanoes have been noted globally ($\delta^{18}O$ ‰ = $[R_{sample}/R_{standard} - 1] \times 1000$, $R = {}^{18}O/{}^{16}O$; standard is Vienna Standard Mean Ocean Water, VSMOW; Baertschi, 1976). Since oxygen

* Corresponding author.
E-mail address: sasm@wwu.edu (M. Sas).

https://doi.org/10.1016/j.jvolgeores.2021.107430

is the most abundant element in magmatic systems, even minor fluctuations (sub-per mil) in $\delta^{18}O$ can amount to large mass transformations resulting from crustal assimilation or mafic influx (Bindeman, 2008). The significant drops (i.e., ~6‰) in magmatic $\delta^{18}O$ ratios following caldera formation have been interpreted to be the result of large-scale incorporation of low-$\delta^{18}O$ hydrothermally-altered volcanic rock into the magmatic system (e.g., Yellowstone; Hildreth et al., 1984; Bindeman and Valley, 2000, 2001; Bindeman et al., 2007). Similarly, some calderas in extensional or rift settings exhibit changes in $\delta^{18}O$ between different caldera-collapse events, which are thought to result from mafic influx and re-melting of isotopically variable roof material (e.g., Southwestern Nevada Volcanic Field; Bindeman and Valley, 2003). Furthermore, in continental arc settings, intra-crystal zoning of $\delta^{18}O$ ratios in quartz have been attributed to assimilation of altered crust shortly prior to a catastrophic caldera eruption (e.g., Toba volcano, Sumatra; Budd et al., 2017). The present study explores $\delta^{18}O$ ratios in quartz phenocrysts from rhyolites from the Okataina Volcanic Centre (OVC), a caldera volcano in Aotearoa New Zealand. This magmatic system has been frequently active on a millennial-scale and is well-studied (e.g., Nairn, 2002; Smith et al., 2005, 2010; Shane et al., 2008a, 2008b). Unlike the volcanoes mentioned above, it is situated in an actively rifting arc where the continental crust is thin (~25 km; Bannister et al., 2004).

Quartz was selected as it is ubiquitous in high-SiO_2 rhyolites from the OVC, and because it is particularly useful for mineral-specific isotopic studies as it commonly abundant, coarse-grained, and resilient to secondary isotope exchange (Bindeman, 2008). At the OVC, quartz and other phenocrysts have revealed considerable insight to the petrogenesis of magmas. The previous examination of zoning, trace element compositions, and melt inclusions in OVC quartz phenocrysts suggest mingling of discrete parental melts as well as rapid crystallization (Shane et al., 2008b; Smith et al., 2010; Matthews et al., 2012). Several zircon U–Th disequilibrium and trace elements studies (e.g., Storm et al., 2011, 2012, 2014; Rubin et al., 2017) identify crystal populations with differing compositional and thermal histories that indicate the presence of long-lived, structurally disconnected magmatic reservoirs. Similarly, the accompanying amphibole population requires repeated remobilization of a thermally zoned system with minimal lateral connectivity (Shane and Smith, 2013). Investigation of oxygen fugacity (fO_2) from Fe–Ti oxides and orthopyroxene compositions called on the presence of cold and wet, as well as hot and dry, rhyolite magmas (Deering et al., 2010). Plagioclase phenocryst cores were found to be antecrystic and nucleate in crustally-contaminated melts of variable compositions (Shane, 2015; Sas et al., 2021). All of these studies indicate the presence of separate but contemporaneous melt bodies in a voluminous crystal mush with restricted lateral connectivity. Furthermore, recent studies examining intra- and whole-crystal Sr–Pb isotopic ratios in plagioclase from OVC rhyolites reveal fairly consistent isotopic signatures over the last ~0.6 My (Sas et al., 2019, 2021). To examine how magmatic records in a later-crystalizing phase compare to those in plagioclase, and to elucidate the effects of open system processes through the lifetime of this dynamic magmatic system, textures and stable oxygen isotopic ratios of quartz were investigated.

Albeit a well-studied region, there are few $\delta^{18}O$-based studies at the OVC and adjacent silicic caldera volcanoes (e.g., plagioclase separates from Maroa Volcanic Centre rhyolites, McCulloch et al., 1994). At the OVC, although Blattner and Reid (1982) and Blattner et al. (1996) provide $\delta^{18}O$ ratios of quartz from some rhyolites, the analyses are of bulk samples (many crystals) and are limited to younger units. This study presents the first single crystal- and intra-crystal- scale $\delta^{18}O$ data in OVC quartz, using secondary ion mass spectrometry and laser fluorination techniques. The sample suite was selected to characterize potential temporal and spatial $\delta^{18}O$ ratio variations at the volcanic centre. Unlike at other caldera centers, this work identifies a well-balanced system at the OVC, with consistent inputs from the mantle and crust, and constant mechanisms of crustal assimilation across the duration of the magmatic system.

2. Geologic Background

The OVC has been active for ~600 ka, erupting dominantly rhyolitic magmas from a locus that has had at least three caldera-collapse events (Nairn, 2002; Cole et al., 2014). The volcanic center is situated within the northeastern segment of the Taupō Volcanic Zone (TVZ) – an actively-rifting, 2 million-year-old volcanic arc that is located in the central North Island, Aotearoa New Zealand (Fig. 1) (Wilson et al., 1995). The TVZ is the 200 km subaerial terminus of the ~3000 km long Tonga-Kermadec volcanic arc and is a result of the westward subduction of the Pacific Plate beneath the Australian Plate (Wilson et al., 1995). The rates of subduction are reduced from northeast offshore North Island, 58 mm/yr, to southwest offshore North Island, 19 mm/yr, as subduction becomes more oblique (Wallace et al., 2009). In addition to subduction-related magma generation, magma production in the TVZ is also impacted by extension-induced crustal thinning (~25 km crystal thickness, Bannister et al., 2004) and concomitant decompression melting of the underlying mantle. The coupled subduction-extension setting results in high rates of magma emplacement within the crust (Stern and Benson, 2011; Cole et al., 2014). The extension rate at the OVC is ~12 mm/yr (Wallace et al., 2004).

The uppermost crust in the TVZ, down to ~3 km depth at the OVC, consists of Pleistocene volcanics and volcaniclastics (Cole et al., 2010, 2014; Seebeck et al., 2010). Underlaying these volcanic rocks, in the middle to upper crust, are interbedded and structurally complex sandstones and mudstones (collectively referred to as greywacke in literature) that have been weakly metamorphosed, albeit higher-grade xenoliths in southern TVZ lavas suggest increased metamorphism in the middle crust (Price et al., 2012, 2015; Milicich et al., 2021). The metasediments comprise two Mesozoic, arc-sourced terranes, the Torlesse Composite Terrane (Jurassic-Cretaceous) to the east and the Waipapa Composite Terrane (Permian-Jurassic) to the west (Fig. 1; Spörli, 1978; Price et al., 2015). The Torlesse Terrane constitutes somewhat equal portions of lithics, quartz and feldspar, with high average SiO_2 contents of ~70 wt% (Reid, 1983; Price et al., 2015). The Waipapa Terrane contains a larger portion of volcanic lithics relative to other components, thereby resulting in lower average SiO_2 contents of ~63 wt% (Reid, 1983; Price et al., 2015). The boundary between the two terranes in debated; Price et al. (2015) suggest an oblique boundary based on the presences of Torlesse xenoliths in dacite lava north of the Taupō Volcanic Centre. Conversely, Milicich et al. (2021) suggest a steeply dipping boundary that crosses through the southern region of the OVC, although uncertainty of the boundary location extends approximately 20 km northwest of the OVC. Notably, Milicich et al. (2021) propose that Quaternary extension has reactivated the boundary between the two metaseimentary terranes, and likely heavily impacted the location of the TVZ. In contrast to middle to upper crust compositions, lower crust compositions below the OVC, and the TVZ in general, are poorly constrained. However, metaigneous xenoliths found in andesite lavas from the southernmost TVZ suggest lower crust rocks are of oceanic crust origin (Graham et al., 1990; Price et al., 2012).

The coupled extension-subduction setting of the TVZ results in strong NE-SW lineaments of structural (e.g., faults and grabens) and volcanic (e.g., fissure eruptions, caldera boundaries) features (Nairn, 2002; Seebeck et al., 2010; Cole et al., 2014). At the OVC, this is apparent by the formation of two parallel vent alignments that are oriented NE-SW, Tarawera to the south and Haroharo to the north (Fig. 1), which formed following the most recent caldera-collapse event at ~45 ka (Cole et al., 2010; Danišík et al., 2012). Tarawera and Haroharo are both composed of predominantly rhyolitic deposits (domes and pyroclastics) that have formed over several eruption periods (Nairn, 2002). Although there are minor mineralogical differences across the OVC (e.g., cummingtonite is the dominant ferromagnesian phase in Haroharo deposits, but is scarce in Tarawera deposits), the majority of deposits are high-SiO_2 rhyolites with cognate plagioclase + quartz

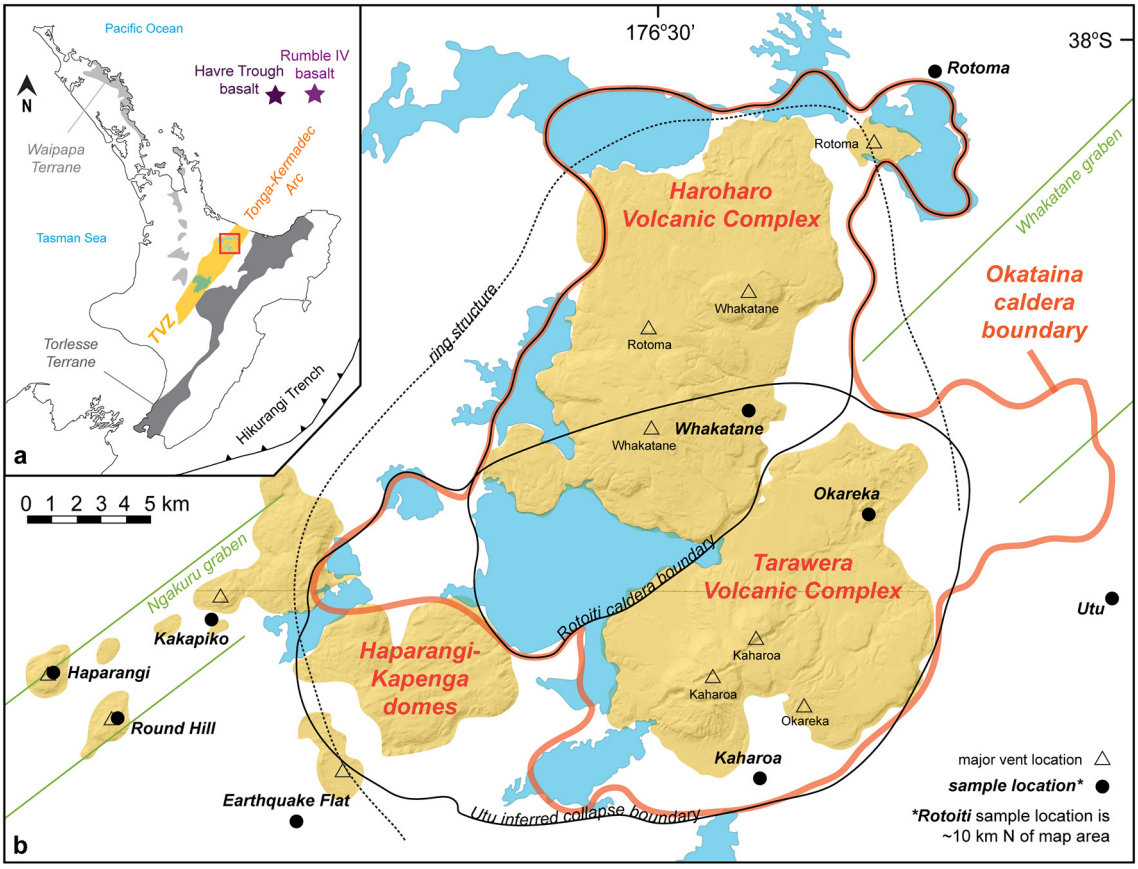

Fig. 1. Map of the Okataina Volcanic Centre (OVC) showing sample locations (circles), major vent locations (triangles), caldera boundaries (thin solid lines), and intra-caldera volcanic complexes and extra-caldera domes (shaded regions). Sample locations are also included in Table 1. The location of the OVC within the Taupō Volcanic Zone (TVZ) and the two regional metasedimentary formations, Torlesse and Waipapa, (Price et al., 2015; Milicich et al., 2021) are shown in the inset map. Okataina inferred caldera boundaries, ring structure (dashed line), dome complexes, and grabens (green lines) are from Nairn (2002). Major vent locations are from Nairn (2002), Nairn et al. (2004), Smith et al. (2006), and Shane et al. (2008a). Locations of basalt samples used for modelling (stars, inset map) are from Graham et al. (1992) and Macpherson et al. (1998).

>> Fe-Ti oxides + amphibole + orthopyroxene ± biotite ± clinopyroxene (Nairn, 2002; Smith et al., 2005).

This study focuses on ten representative rhyolitic units from seven spatially, temporally and volumetrically varied eruptive episodes that cover the span of eruptive activity at the OVC and include caldera-forming eruptions, as well as intra-caldera and extra-caldera eruption episodes (Table 1, Fig. 1). The caldera-forming eruptions include Utu, the oldest known collapse event (~557 ka; Leonard et al., 2010), and Rotoiti, the most recent significant collapse event (~45 ka; Nairn, 2002; Shane et al., 2005). Intra-caldera small volume eruptions consist of Rotoma (9.5 ka) and Whakatane (5.5 ka) from Haroharo, and Okareka (21.8 ka) and Kaharoa (0.7 ka) from Tarawera (Nairn, 2002; Smith et al., 2005, 2006). Extra-caldera small volume eruptions consist of the Round Hill, Haparangi, and Kakapiko domes, which are part of the Haparangi-Kapenga dome complex (~200–100 ka) that preceded Rotoiti (Nairn, 2002). One additional unit, Earthquake Flat, erupted weeks to months post-Rotoiti, with vents along the southwestern edge of the OVC ring structure (Nairn and Kohn, 1973). Earthquake Flat and the extra-caldera domes contain coarser crystals (≤4 mm) and are also more crystal-rich (20%–40%) than intra-caldera deposits (generally ≤2 mm crystals and ≤15% crystals), and may represent remobilized portions of a mostly-crystalline reservoir (Molloy et al., 2008; Sas et al., 2021). With the exception of a few dacitic Earthquake Flat clasts, all units fall in the rhyolite field on a total alkali silica diagram (Fig. 2). In units where detailed stratigraphy is available, stratigraphic units selected from each deposit represent the most volumetrically significant unit and/or represent hybrid magmatic products that consist of mingled or mixed rhyolitic melts (Table 1 and references therein). The studied units are summarized in Table 1 and sample locations are shown in Fig. 1.

3. Methods

3.1. Sample preparation

The samples studied here are all previously collected (Table 1 and references therein) non-altered juvenile tephras or non-welded, juvenile ignimbrites whose loose nature required minimal pressure to liberate the crystals (Sas et al., 2021). Following liberation, several hundred crystals, which exhibited a bipyramidal habit and were >100 μm in size, were individually picked from each unit using a binocular microscope. Any crystals exhibiting surface alteration were avoided. For *in-situ* secondary ion mass spectrometry (SIMS) analyses, untreated crystals were mounted onto a single 1-in. diameter epoxy plug, with standard crystals (NBS28) imbedded in the center of the plug. Crystals were grinded to expose crystal cores, and a sub-micron polish was applied to the plug. For whole-crystal laser fluorination (LF) analyses, non-weathered, inclusion-free quartz crystals were selected using a high-magnification binocular microscope where possible. For units where inclusions were unavoidable (Rotoiti and Kaharoa; Smith et al., 2010), a low total inclusion volume was achieved based on high-magnification optical examination and measurement of melt inclusions using a microscale. Specifically, for Kaharoa, <1 vol% was obtained due to the paucity and size of the inclusions in individual crystals, and for

Table 1
Summary of rhyolitic OVC units.

Eruption	Kaharoa	Whakatane	Rotoma	Okareka	Earthquake Flat	Rotoiti	Kakapiko	Haparangi	Round Hill	Utu
Eruption style	Dome	Dome	Dome	Dome	Dome	Caldera	Dome	Dome	Dome	Caldera
Age (ka)	0.7	5.5	9.5	21.8	~45	45	200–45	200	200–45	557
Volume (km^3)[a]	9.1	11.3	8	5	10	120	–	–	–	90
Strat unit[b]	T2(1)	WT1(7)	RT2(7,9)	T1(10)	–	T1(15)	–	–	–	–
SiO_2[c]	76.44	76.60	76.38	75.98	72.24	73.66	73.94	73.68	74.15	73.44
T (°C)[d]	724 ± 16	745 ± 11	760 ± 9	794 ± 12	754 ± 52	766 ± 13	722 ± 13	718 ± 15	724 ± 13	762 ± 8
P (kbar)[e]	0.6–2.5	0.7–2.8	0.7–1.9	0.8–1.8	0.7–1.4	0.6–2.5	–	–	–	–
fO_2 (NNO)[f]	+0.00 ± 0.54	+0.34 ± 0.08	+0.62 ± 0.06	+0.82 ± 0.08	−0.26 to +0.32	+0.92 ± 0.09	−0.19 ± 0.10	−0.47 ± 0.12	−0.28 ± 0.11	−0.52 ± 0.10
H_2O[g]	5.18^{Qmi}	4.48^{Qmi}	5.26^{Qmi}	5.12^{Qmi}	5.04^{Pmi}	4.99^{Qmi}	3.97^{g}	5.07^{g}	3.87^{g}	–
Mineral assemblage[h]	plg > qtz>> bio > Fe-Ti ± hbl, opx, cgt	qtz > plag>> hbl > cgt> Fe-Ti > opx	plg > qtz>> Fe-Ti > opx > cgt	plg > qtz>> opx + hbl + cgt + Fe-Ti>> bio	plg > qtz>> bio > hbl> Fe-Ti ± opx	plg > qtz>> cgt > Fe-Ti > hbl > opx	qtz > plg>> bio > hbl > opx + Fe-Ti	qtz > plg>> bio>> hbl> opx + Fe-Ti	qtz > plg>> bio > hbl > opx + Fe-Ti	qtz/plg> bio>> hbl> opx + Fe-Ti
$\delta^{18}O$ analyses[i]	SIMS (n = 7), LF (n = 2)	LF (n = 3)	SIMS (n = 7), LF (n = 2)	LF (n = 3)	LF (n = 2)	SIMS (n = 8), LF (n = 2)	LF (n = 3)	LF (n = 8)	LF (n = 3)	SIMS (n = 7), LF (n = 2)
Location[j]	−38.273, 176.515	−38.140, 176.515	−38.017, 176.590	−38.185, 176.546	−38.299, 176.277	−37.922, 176.342	−38.233, 176.205	−38.207, 176.223	−38.260, 176.239	−38.204, 176.660
References[k]	1–4	5–8	7–9	6, 8, 10	11–14	9, 15–17	6, 18	18	18	6, 19–22

[a] Volumes extracted from literature are dense rock equivalent (DRE).
[b] Stratigraphic unit from which crystals were extracted (where available) are based on subdivisions established by the respective study, which is included as a number in parentheses following the unit and is listed below in References[k]. Stratigraphic units selected are the most volumetrically significant and/or hybrid magmatic products.
[c] Average whole rock SiO_2 contents extracted from literature.
[d-f] Representative unit Fe–Ti oxides temperatures (± 2sd) and fO_2 (± 2sd) extracted from literature, and amphibole pressure ranges from Shane and Smith (2013).
[g] H_2O contents extracted from literature. *Qmi*: H_2O from quartz-hosted melt inclusions, *Pmi*: H_2O from plagioclase-hosted melt inclusions, *g*: estimated H_2O from glass.
[h] Mineral abbreviations are: *plg*: plagioclase, *qtz*: quartz, *bio*: biotite, *hbl*: hornblende, *cgt*: cummingtonite, *opx*: orthopyroxene, *Fe-Ti*: Fe–Ti oxides.
[i] Analyses include intra-crystal secondary ion mass spectrometry (SIMS) and whole-crystal laser fluorination (LF); n is the total number of crystals analyzed per method.
[j] Locations of samples are provided in decimal degrees.
[k] 1: Nairn et al. (2004); 2: Leonard et al. (2002); 3: Sahetapy-Engel et al. (2014); 4: Hogg et al. (2003); 5: Kobayashi et al. (2005); 6: Nairn (2002); 7: Smith et al. (2006); 8: Lowe et al. (2008); 9: Smith et al. (2005); 10: Shane et al. (2008a); 11: Molloy et al. (2008); 12: Nairn and Kohn (1973); 13: Froggatt and Lowe (1990); 14: Davis (1985); 15: Shane et al. (2005); 16: Schmitz and Smith (2004); 17: Danišík et al. (2012); 18: Sas et al. (2021); 19: Cole et al. (2010); 20: Cole et al. (2014); 21: Leonard et al. (2010); 22: Deering et al. (2010).

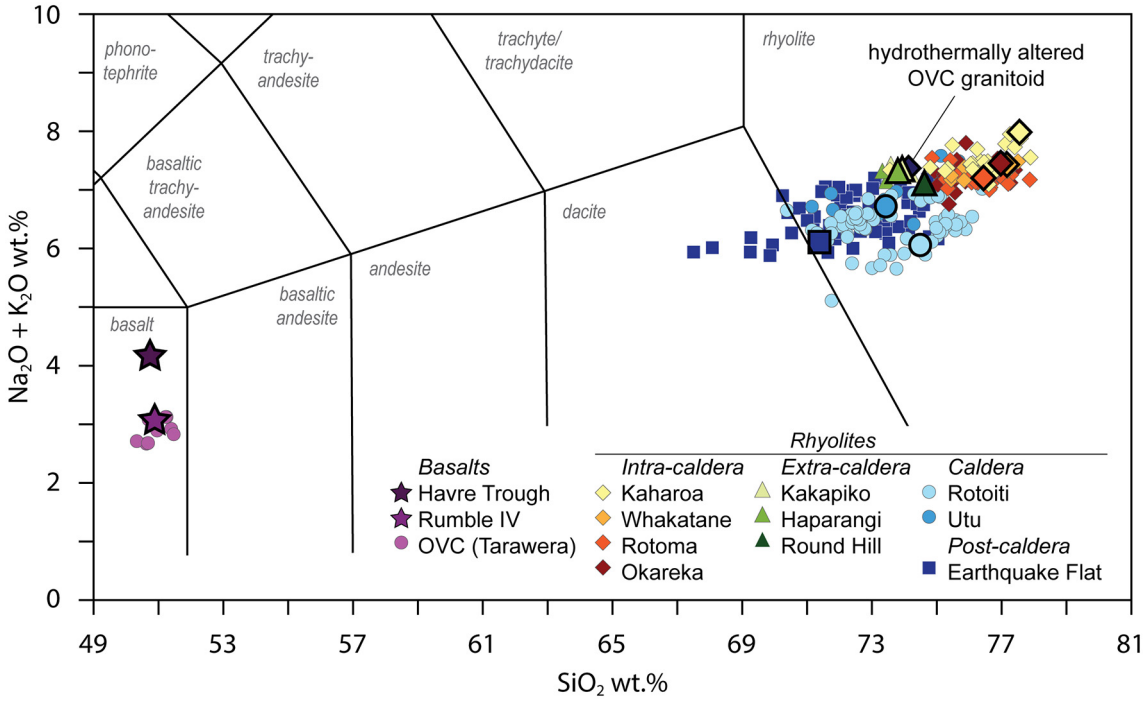

Fig. 2. Total alkali silica (TAS) diagram of OVC rhyolite units included in this study (whole rock; Leonard et al., 2002; Nairn, 2002; Schmitz and Smith, 2004; Smith et al., 2006; Molloy et al., 2008; Shane et al., 2008a; Deering et al., 2008; Shane and Smith, 2013; Sas et al., 2021), basalt samples used for modelling (Havre Trough and Rumble IV, whole rock; Gamble et al., 1994), a representative OVC basalt (Tarawera, whole rock; Gamble et al., 1993; Nairn, 2002; Nairn et al., 2004; Hiess et al., 2007; Zellmer et al., 2020), as well as a hydrothermally altered granitoid found in OVC rhyolite (TW1, whole rock; Brown et al., 1998). Rhyolite samples from which quartz crystals were extracted have enlarged symbols and a thick, black outline.

Rotoiti, <2 vol% was achieved. Since Rotoiti crystals contain fresh, unaltered (sealed) melt inclusions (Smith et al., 2010), their contribution to $\delta^{18}O$ is considered to be insignificant (Bindeman and Valley, 2002). In order to remove any attached glass or unsealed inclusions, quartz crystals analyzed using LF were first purified by etching in 30% hydrofluoric acid for 5 min, following the technique of Bindeman and Valley (2002). A summary of units analyzed, methods employed, and total number of crystals per unit are included in Table 1.

3.2. Cathodoluminescence imaging and in situ oxygen isotope analysis

Cathodoluminescence (CL) images of quartz crystals were obtained using a Gatan Mini-CL installed on a field emission scanning electron microscope (FE-SEM; JEOL JSM-7000F at Hokkaido University). Between 25 and 30 crystals per unit were imaged using SEM-CL, and brightness and contrast settings were maintained across all images for comparison of textures. A 15 kV accelerating voltage and a current of 10 nA was employed in our study. The polished section was coated with a carbon thin film (~20 nm).

Analyses of $\delta^{18}O$ zones in individual quartz crystals from four pilot units were obtained by *in situ* O-isotope measurements using a SIMS instrument (CAMECA IMS-1280HR at Hokkaido University). Units selected for SIMS analyses consist of two large-volume eruptions, Utu and Rotoiti, and two small-volume intra-caldera eruptions, Rotoma and Kaharoa (Table 1). Quartz textures were first examined using SEM-CL imaging. Then, ideal (i.e., complete sections from core to rim where possible) and 7–8 representative crystals were selected for SIMS analyses, where zones with differing CL intensities (brightness) were analyzed. Before measurements, the polished section was coated with a gold thin film (~70 nm).

The SIMS measurements were performed during two different sessions with different analytical precisions. Procedures essentially followed those described in Kawasaki et al. (2018). For one set of analyses (low-precision mode), a $^{133}Cs^{+}$ primary beam (20 keV, 1 nA) with a diameter of ~6 μm was used. Negative secondary ions, $^{16}O^{-}$ and $^{18}O^{-}$, were measured simultaneously in multi-collection mode using two Faraday cups. A normal incident electron flood gun was used for electrostatic charge compensation of the analyzed area during the analyses. The mass resolution of $M/\Delta M$ was set at ~2200. The secondary ion intensity of $^{16}O^{-}$ was typically ~1.0×10^9 cps. Before the analyses, the analyzed area was sputtered with a rastered beam of ~11 μm for 30 s. Each analysis consisted of 5 cycles of collecting the secondary ions for 3 s. NBS28 ($\delta^{18}O$ = 9.29‰, Kusakabe and Matsuhisa, 2008), imbedded in the center of the sample plug, was used as a standard for correcting instrumental mass fractionation (IMF). Because of some heterogeneity of $\delta^{18}O$ among grains of the NBS28 standard (e.g., Appleby et al., 2008), we measured multiple grains of the NBS28 standard for every bracketing (to account for this heterogeneity). Every analytical cycle consisted of 10 analyses of NBS28, 10 analyses of samples, and 10 analyses of NBS28. The data were then corrected using a standard bracketing method using NBS28 and normalizing to $\delta^{18}O$ = 9.29‰ (Kusakabe and Matsuhisa, 2008). Uncertainty of the IMF correction was 0.15–0.27‰. Analytical errors were typically ~0.43‰ 2σ in $\delta^{18}O$, including a statistical error of individual analysis calculated from counting statistics of total ion counts and the uncertainty of the IMF correction. The reproducibility of repetitive analyses of a single grain of the NBS28 standard was 0.54‰ (2 standard deviation, n = 10). Analyzed spots were carefully observed by FE-SEM.

For another set of the analyses (high-precision mode), a $^{133}Cs^{+}$ primary beam (20 keV, 2 nA) with a diameter of ~9 μm was used. The secondary ion intensity of $^{16}O^{-}$ was typically ~2.0×10^9 cps. Before the analyses, the analyzed area was sputtered with a rastered beam of ~14 μm for 30 s. Each analysis consisted of 10 cycles of collecting the secondary ions for 10 s. Other settings were identical to those of the low-precision mode. The IMF correction with bracketing analyses of the NBS28 standard could not be readily applied for the high-precision

mode, because both the heterogeneity of NBS28 and background drift of Faraday cup detectors were significant in this mode. Averages of $\delta^{18}O$ ratio for each sample analyzed in high-precision mode were normalized to averages of $\delta^{18}O$ ratios for the same sample analyzed in low-precision mode, corrected by multiple bracketing. We note that the high-precision mode was applied to reveal the degree of homogeneity/heterogeneity of samples with an improved reproducibility. Analytical errors were typically ~0.16‰ (2σ) in $\delta^{18}O$, including a statistical error of individual analysis calculated from counting statistics of total ion counts and the uncertainty of the normalization. The reproducibility of repetitive analyses of a single grain of the NBS28 standard was 0.23‰ (2sd, $n = 10$).

3.3. Laser fluorination (LF) analytical procedure

Quartz phenocrysts from all of the samples (Table 1) were analyzed using LF (Sharp, 1990). Aliquots of quartz weighing between 1 and 2 mg (dominantly representing a single crystal) were analyzed at the Stable Isotope Laboratory, University of Oregon, following the CO_2-LF methods of Bindeman (2008). Samples were fluorinated using BrF_5 and a CO_2 laser. Following reaction, O_2 gas was cryogenically purified, cleaned of excess F_2 using liquid Hg vapors, and converted to CO_2, which was analyzed for oxygen isotopic compositions using a stable isotope ratio mass spectrometer (Thermo Finnigan MAT 253). A University of Oregon garnet (UOG) with $\delta^{18}O = 6.52$‰ VSMOW (Troll et al., 2013) was used as a standard to correct unknowns to VSMOW scale (corrections were 0.10–0.20‰) with 0.11–0.13‰ (2sd) external reproducibility across the analytical sessions.

4. Results

4.1. Quartz textures

Approximately 100 crystals from the four samples (Kaharoa, Rotoma, Rotoiti and Utu; Table 1) examined via SEM-CL imaging exhibit similar textures that are typical of magmatic quartz (e.g., Wilcock et al., 2013). All of the quartz crystals display weak oscillatory zoning of bright (high CL intensity) and dark (low CL intensity) bands that range from 5 to 100 μm in width (Fig. 3; Supplementary Fig. A1–A4). One exception is a single Utu crystal that exhibits diffuse boundaries between zones (Fig. 3h). Quartz crystals can be divided into three broad categories based on variations in CL brightness between cores and rims: (1) subtle differences in brightness between the core and rim (Q1; e.g., Fig. 3c); (2) notably brighter cores with darker rims (Q2; e.g., Fig. 3b); and (3) notably darker cores with brighter rims (Q3; e.g., Fig. 3e). The boundaries between quartz core/mantle and rim zones are consistently resorbed (i.e., truncated growth patterns). These textural groups are found in the Kaharoa, Rotoma, Rotoiti and Utu samples (Table 1; Supplementary Fig. A1–A4), with Q1 being the most common (~40%), and Q2 and Q3 having roughly equal distributions (~30% each). The same

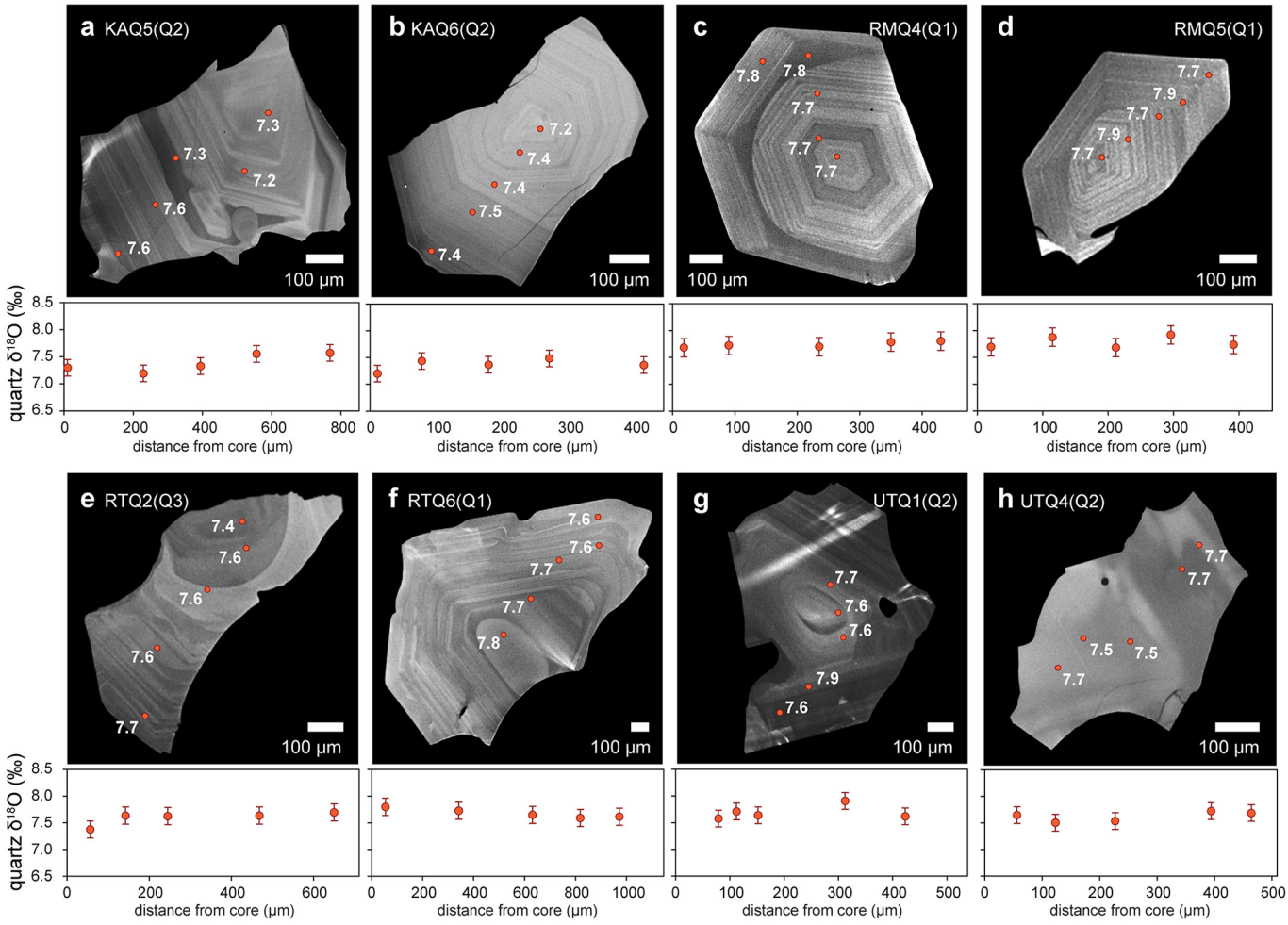

Fig. 3. Cathodoluminescence (CL) images showing high-precision secondary ion mass spectrometry (SIMS) $\delta^{18}O$ analyses of representative OVC quartz crystals from (a–b) Kaharoa, (c–d) Rotoma, (e–f) Rotoiti, and (g–h) Utu. The error bars represent the respective 2σ for each analysis. SIMS $\delta^{18}O$ analyses and their respective 2σ are listed in Table 2, and all crystals analyzed for each unit are shown in Supplementary Figs. A1–A4. Quartz crystals imaged using CL and analyzed using SIMS were not modified or treated before being embedded in epoxy.

textures are observed in previous studies of Okareka and Rotoiti quartz (Shane et al., 2008a; Smith et al., 2010), but differ slightly from Earthquake Flat quartz CL images (Smith et al., 2010; Matthews et al., 2012), some of which show a bright CL band on the crystal rims in addition to the aforementioned textures.

Although quartz crystals exhibit similar textures in the samples, the core zones differ. Specifically, Utu quartz cores are commonly bright (i.e., Q2), and some cores exhibit resorption surfaces that have a mixture of bright and dark intensities (e.g., Fig. 3g). In contrast, Rotoiti quartz crystals commonly have dark cores (i.e., Q3; Fig. 3e). Other Rotoiti cores, as well as many Rotoma cores, exhibit little to no difference in brightness between cores and rims (i.e., Q1; Fig. 3c–d,f). Kaharoa cores, similarly to Utu, are mostly bright (i.e., Q2; Fig. 3a–b), and several cores display a complex mixture of bright and dark intensities.

4.2. Oxygen isotopic compositions

Intra-crystal $\delta^{18}O$ data obtained via SIMS for the four pilot units (Utu, Rotoiti, Rotoma, and Kaharoa) are listed in Table 2, with examples of crystals and their respective SIMS analyses shown in Fig. 3, and all crystals and SIMS analyses shown in Supplementary Figs. A1–A4. We analyzed 5–6 spots in each crystal from zones of variable CL intensity. Two crystals from each of Utu, Rotoma, and Kaharoa, and five crystals from Rotoiti, yielded intra-crystal homogeneity better than the analytical reproducibility of the NBS28 standard in high precision mode (0.23‰, 2σ) (Table 2).

To assess potential variations between different quartz grains in each sample, a total of seven to eight crystals were examined per sample in a faster but lower-precision mode, analyzing 3 spots in each crystal. Quartz from all four samples exhibited inter-crystal $\delta^{18}O$ homogeneity at a level similar to the analytical reproducibility of the NBS28 standard (0.54‰, 2σ) (Table 2). To further investigate sample-scale isotopic variability, the data were modelled as Gaussian distribution curves using kernel density estimation (KDE), with maximum analytical uncertainty (~0.5‰, 2σ) set as the bandwidth (Fig. 4). The standard deviation produced by the Gaussian models (0.6–0.7‰) is similar to the analytical uncertainty, indicating isotopic homogeneity within each sample is mostly within the resolution of this low-precision instrumental mode. The units do exhibit variation among modelled means, although they overlap within error (Fig. 4). Assuming relative inter-crystal homogeneity, two additional whole crystals from each sample were analyzed using the more precise LF technique (Table 3, Fig. 5). Within-sample $\delta^{18}O$ homogeneity is indicated by these sub-samples of quartz (1–2 mg, commonly representing a single crystal). Analyses are listed in Table 3 and shown in Fig. 5.

Finally, the means of the analytical methods, SIMS and LF, are in good agreement and within analytical uncertainty of one another (Fig. 5). Moreover, both methods point to $\delta^{18}O$ homogeneity (within SIMS error, ~0.5‰, 2σ) across the four units studied (Fig. 5). Quartz homogeneity within and between units is also observed across the additional six units analyzed using high precision LF (Table 3). However, there is one outlier beyond the LF analytical error: a Haparangi crystal with notably lower ratios (by 1.14‰) than the unit mean (Table 3).

5. Discussion

5.1. Implications of quartz $\delta^{18}O$ homogeneity

Changes in $\delta^{18}O$ ratios up to ~6‰ have been reported in magmas from rhyolite volcanoes following caldera formation (e.g., Bindeman and Valley, 2001). This is not evident for the OVC. At intra-crystal-scale, $\delta^{18}O$ homogeneity across differing textural growth zones are within analytical error (~0.2‰, 2σ) (Table 2, Fig. 3). Thus, during the pre-eruptive amalgamation of separate magma batches into the eruptible magma as envisaged by previous workers (e.g., Shane et al., 2005, 2008b; Smith et al., 2006, 2010; Shane, 2015), the $\delta^{18}O$ ratios of quartz

Table 2
Intra-crystal MC-SIMS $\delta^{18}O$ (‰) analyses of OVC quartz.

Unit/Crystal[a]	distance[b]	$\delta^{18}O$	2σ[c]	Unit/Crystal[a]	distance[b]	$\delta^{18}O$	2σ[c]
OVC rhyolites							
Kaharoa				RTQ-2	56	7.37	0.16
KAQ1	64	7.53	0.44		142	7.64	0.16
	222	7.62	0.44		245	7.63	0.16
	395	7.72	0.44		468	7.64	0.16
KAQ2	128	7.18	0.40		650	7.70	0.16
	422	7.42	0.40	RTQ-2	99	7.59	0.40
	672	7.19	0.40	repeat	311	7.65	0.40
KAQ3	30	7.47	0.42		577	7.79	0.40
	507	7.78	0.42	RTQ-3	21	7.77	0.16
	653	7.64	0.42		93	7.78	0.16
KAQ4	53	7.03	0.46		255	7.76	0.16
	415	7.40	0.46		379	7.86	0.16
	670	7.77	0.46		544	7.91	0.16
KAQ-5	10	7.30	0.15	RTQ-3	66	7.42	0.41
	229	7.19	0.15	repeat	333	7.41	0.41
	394	7.33	0.15		525	7.16	0.41
	556	7.55	0.15	RTQ4	94	7.76	0.41
	768	7.57	0.15		312	7.99	0.40
KAQ-5	61	7.46	0.42		702	8.12	0.40
repeat	389	7.07	0.42	RTQ-5	41	7.71	0.16
	717	7.03	0.42		131	7.69	0.16
KAQ-6	11	7.20	0.15		286	7.72	0.16
	78	7.44	0.15		414	7.70	0.16
	179	7.37	0.15		606	7.66	0.16
	271	7.48	0.15	RTQ-5	143	7.49	0.45
	414	7.36	0.15	repeat	326	7.58	0.45
KAQ-6	14	7.97	0.44		563	7.53	0.45
repeat	270	7.11	0.44	RTQ-6	54	7.80	0.16
	397	7.53	0.44		342	7.73	0.16
KAQ7	79	7.30	0.43		631	7.65	0.16
	386	6.94	0.43		819	7.59	0.16
	590	7.33	0.43		972	7.62	0.16
Rotoma				RTQ-6	90	7.86	0.43
RMQ1	21	7.95	0.44	repeat	536	7.57	0.43
	105	8.07	0.44		880	7.25	0.44
	186	7.60	0.44	RTQ7	30	7.86	0.42
RMQ2	80	7.92	0.40		190	8.01	0.42
	216	7.67	0.39		334	7.58	0.42
	515	7.55	0.39	RTQ8	74	7.83	0.46
RMQ3	50	7.69	0.41		268	7.84	0.46
	217	8.21	0.41		420	7.71	0.46
	435	7.69	0.41	*Utu*			
RMQ-4	18	7.68	0.17	UTQ-1	79	7.58	0.16
	90	7.72	0.17		112	7.71	0.16
	235	7.70	0.17		152	7.64	0.16
	350	7.78	0.17		312	7.91	0.16
	430	7.80	0.17		423	7.62	0.16
RMQ-4	105	7.48	0.39	UTQ-1	28	7.46	0.44
repeat	253	7.82	0.39	repeat	265	7.69	0.44
	400	7.42	0.39		323	7.77	0.44
RMQ-5	21	7.70	0.17	UTQ2	14	7.70	0.41
	115	7.88	0.17		225	7.64	0.41
	212	7.68	0.17		436	7.38	0.41
	296	7.92	0.17	UTQ3	51	7.71	0.42
	392	7.74	0.17		191	8.31	0.42
RMQ-5	57	8.43	0.44		280	7.53	0.43
repeat	189	7.88	0.44	UTQ-4	56	7.65	0.16
	369	7.51	0.44		123	7.50	0.16
RMQ6	116	7.11	0.44		227	7.53	0.16
	229	7.54	0.44		394	7.72	0.16
	535	7.97	0.44		464	7.69	0.16
RMQ7	76	7.81	0.43	UTQ-4	130	7.55	0.40
	203	7.83	0.43	repeat	330	8.03	0.40
	297	8.46	0.44		486	7.96	0.40
Rotoiti				UTQ5	75	7.59	0.42
RTQ-1	42	7.54	0.16		246	7.45	0.42
	91	7.63	0.16		417	8.14	0.43
	185	7.64	0.16	UTQ6	62	7.45	0.44
	315	7.51	0.16		442	7.40	0.44
	524	7.61	0.16		701	7.50	0.45
	897	7.49	0.16	UTQ7	56	7.28	0.45
					256	7.77	0.45
					356	7.42	0.45

Table 2 (*continued*)

Unit/Crystal[a]	distance[b]	$\delta^{18}O$	2σ[c]	Unit/Crystal[a]	distance[b]	$\delta^{18}O$	2σ[c]
Reproducibility of NBS-28 Standard							
		2SD (*n*)					
Low-precision mode		0.54 (10)					
High-precision mode		0.23 (10)					

[a] Repeat analyses represent duplicate analyses of the crystal in low-precision mode.
[b] Analyses are listed in the order from core to rim, with distance from the core provided in μm.
[c] $2\sigma < 0.20$ indicate analyses completed in high-precision mode, and $2\sigma > 0.35$ indicate analyses completed in low-precision mode.

indicate neither significant assimilation of hydrothermally altered roof rocks nor that influx of isotopically distinct melts from deeper in the system occurred (i.e., mantle-derived melts; e.g., Bindeman and Valley, 2003; Budd et al., 2017). Inter-crystal isotopic homogeneity is also observed and demonstrates that the parental reservoirs of the discrete melts from which the quartz crystals are derived (e.g., Shane et al., 2008b; Smith et al., 2010) display considerable overlap in $\delta^{18}O$ ratios (based on the differing textural patterns of crystals, i.e., cores versus rims). This suggests a spatial $\delta^{18}O$ uniformity (to within 0.5‰, 2σ) across the OVC plumbing system. A similar uniformity in radiogenic isotopic ratios is observed in plagioclase, an earlier crystallizing phase, extracted from the same OVC rhyolite units. Specifically, based on plagioclase textures and trace element contents, Sas et al. (2021) determined that plagioclase from the rhyolites nucleated from more mafic melts (albeit not basalts), while plagioclase rims grew in equilibrium with silicic melts. Despite these findings, core and rim Sr–Pb isotopic ratios of plagioclase were largely homogeneous, indicating that the OVC reservoir reached this level of isotopic homogeneity prior to rhyolite formation. The observed homogeneity spans ~550 thousand years and demonstrates temporal $\delta^{18}O$ and Sr–Pb isotopes uniformity in the magmatic system. These observations suggest that the OVC magmatic system has maintained a relatively consistent balance between mantle and crustal mass contributions.

The same $\delta^{18}O$ homogeneity is further supported by the additional six samples analyzed via LF, as variations between the means of all ten units analyzed in this study are within analytical error (≤0.5‰, 2sd) (Tables 2 and 3; Fig. 5). The new $\delta^{18}O$ data (Tables 2 and 3) are similar to reported quartz $\delta^{18}O$ ratios from the OVC based on aliquots of bulk quartz (5–30 mg; Blattner et al., 1996) (Fig. 5), supporting the overall observation of isotopic uniformity. We note a lava dome outside the caldera rim (Haparangi; Fig. 1) contains an outlier crystal that is beyond the uncertainty of the sample mean (Fig. 5). The Haparangi outlier has a lower $\delta^{18}O$ ratio (6.7‰) than other crystals in this study (Table 3; Fig. 5). Hydrothermal alteration may have led to the lower ratio in the Haparangi outlier. Evidence of subsurface hydrothermal alteration of rocks (e.g., comagmatic granitoid lithics found in ignimbrites) in the TVZ is sparse ($n = 3$; Brown et al., 1998), although a granitoid lithic from Kaharoa with low $\delta^{18}O$ ratios (2.8 ± 1.1‰, adjusted to NBS28 ratios in this study; Supplementary Table A1) indicates that interaction between shallow magmatic bodies and meteoric water is possible (Shane et al., 2012). Bindeman (2008) demonstrated that hydrothermal alteration generally leads to more erratic $\delta^{18}O$ ratios throughout crystal populations, while the Haparangi sample population is relatively uniform (mean of 7.8 ± 0.3‰, 2sd, $n = 7$). Therefore, it is possible that the Haparangi outlier ratio represents crystallization in a melt that experienced less crustal assimilation or interaction with mafic influx. Alternatively, it is also possible that incorporation of hydrothermally altered materials is volumetrically sparse, and/or that the ratios of hydrothermally altered materials (1.5–3.1‰, adjusted; Brown et al., 1998) are too moderate to significantly impact the isotopic ratios of OVC magmas, as is explored below.

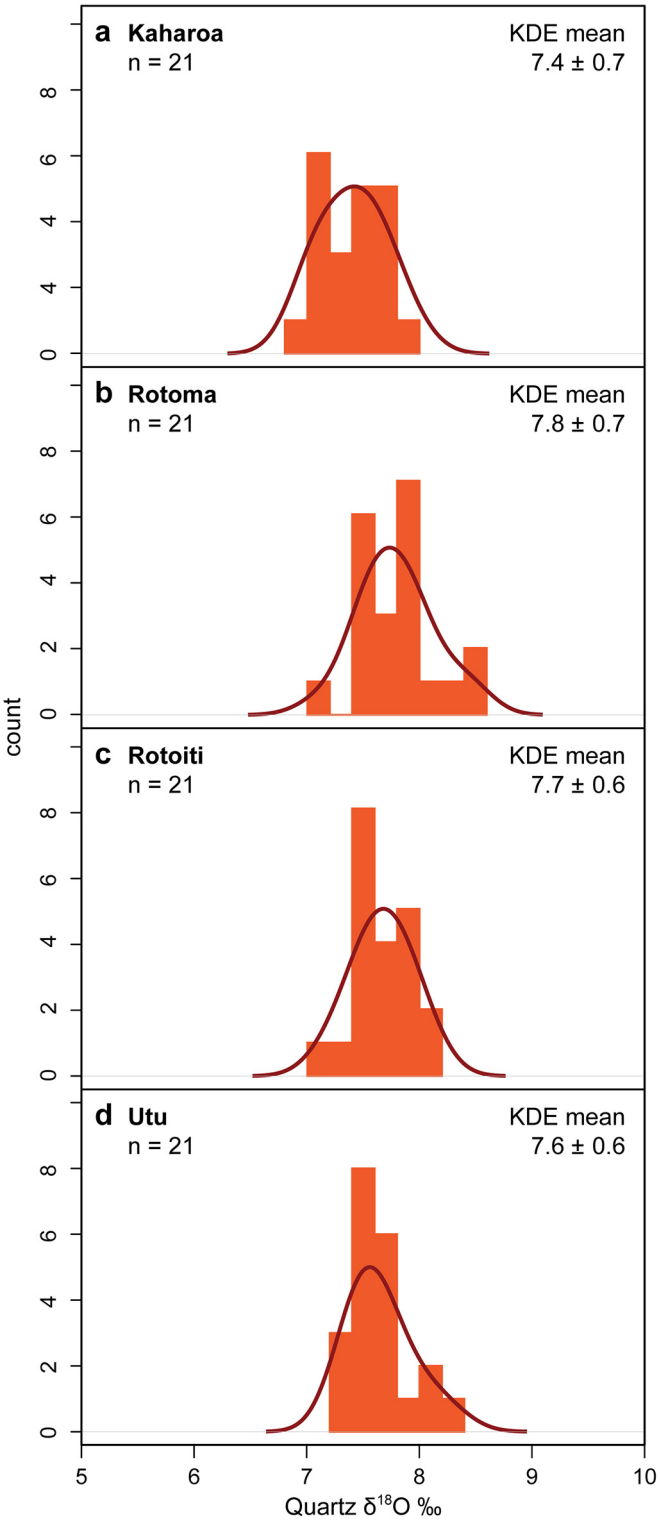

Fig. 4. Low-precision SIMS $\delta^{18}O$ analyses for (a) Kaharoa, (b) Rotoma, (c) Rotoiti, and (d) Utu, modelled by Gaussian distribution curves using kernel density estimation (KDE), with maximum analytical uncertainty ($\pm$ 0.54 2σ) set as the bandwidth. Similarity between modelled KDE and SIMS analytical error indicates intra-unit homogeneity with the resolution of this study.

5.2. Crustal contamination and rhyolite magma genesis at OVC

Recent models for rhyolite petrogenesis, including those for the OVC, include: (1) fractionating basaltic parental melts that experience some

Table 3
Laser fluorination analyses of OVC quartz.

$\delta^{18}O$ (‰)	2sd	$\delta^{18}O$ (‰)	2sd	$\delta^{18}O$ (‰)	2sd
OVC rhyolites					
Kaharoa		*Earthquake Flat*		*Haparangi*	
7.72	0.11	7.80	0.13	6.68	0.11
7.55	0.11	7.71	0.13	7.63	0.11
Whakatane		*Rotoiti*		7.83	0.13
7.48	0.13	7.78	0.11	7.72	0.13
7.65	0.13	7.61	0.11	8.02	0.13
7.53	0.13	*Utu*		7.91	0.13
Rotoma		7.77	0.11	7.92	0.13
7.73	0.11	7.96	0.11	7.72	0.13
7.63	0.11	*Kakapiko*		*Round Hill*	
Okareka		7.77	0.13	7.40	0.13
7.42	0.13	7.28	0.13	7.55	0.13
7.73	0.13	7.27	0.13	7.41	0.13
7.64	0.13				
UOG standard					
	Reported[a]	Analyzed	± 2sd (n)		
Session I	6.52	6.53	0.11 (3)		
Session II	6.52	6.55	0.13 (3)		

[a] (Troll et al., 2013).

degree of crustal contamination (via assimilation of crust and/or mixing with crustal melts), (2) magmatic storage largely consisting of a crystalline mush zone with melt(s) accumulation near the roof of the system, sometimes in semi-isolated bodies, and (3) magmatic rejuvenation through heat, volatile, and/or mass transfer that are provided from mantle-derived melts that underlie the silicic reservoir (e.g., Hildreth, 2004; Bachmann and Bergantz, 2004, 2008a, 2008b; Shane et al., 2008a; Smith et al., 2010; Bachmann and Huber, 2016). Constraining magma sources via radiogenic isotopes is challenging at the OVC due to the overlap of isotopic ratios of TVZ rhyolites and basalts, and the likely basement lithologies involved (Graham et al., 1992; McCulloch et al., 1994; Gamble et al., 1996; Price et al., 2015). However, $\delta^{18}O$ ratios of the likely dominant basement lithology (Mesozoic Torlesse Terrane metasediments, ≥ 9‰) and TVZ basalts (5.3–6.8‰) (Blattner and Reid, 1982; McCulloch et al., 1994) do not overlap (Fig. 5) ($\delta^{18}O$ ratios from literature have been adjusted to the NBS28 ratio used in this study; Supplementary Table A1). Hence, OVC quartz $\delta^{18}O$ ratios may elucidate mantle versus crustal contributions to the magmatic system.

Work by Graham et al. (1992) has demonstrated that, compositionally and isotopically, Waipapa metasediments are not ideal dominant crustal assimilants for TVZ magmas. Early models suggested that the $\delta^{18}O$ ratios of TVZ rhyolites are too low to reflect substantial assimilation of Torlesse Terrane metasediments (i.e., Blattner and Reid, 1982; Graham et al., 1992). In contrast, other work using radiogenic and stable isotopes demonstrate that Torlesse-like compositions serve as ideal assimilants for TVZ magmas (Gamble et al., 1990, 1993; McCulloch et al., 1994; Macpherson et al., 1998). Specifically, Gamble et al. (1993) suggest that TVZ basalts result from ≤10% Torlesse crustal contamination of a primitive TVZ basalt. For rhyolites, McCulloch et al. (1994) suggest as much as 25% crustal contamination of a basaltic parent based on Sr-Nd-Pb-O isotopes of mineral separates (Maroa Volcanic Centre rhyolites).

Recent work reexamined assimilation-fractional crystallization (AFC) and mixing processes at the OVC based on whole rock compositions, Sr–Pb isotopes, and plagioclase Sr–Pb isotopes (Sas et al., 2021). AFC and mixing models of Sas et al. (2021) call on ≥20–30% assimilation of a Torlesse-like crustal source by a mid-ocean ridge (MOR)-like mantle source (DMM) with varying amounts of subduction flux. To test whether models using quartz $\delta^{18}O$ ratios are consistent with models based on radiogenic isotopes, we modelled simple mixing between basaltic parental melts and Torlesse-like metasediments. The $\delta^{18}O$ ratios of potential crystallization melts were calculated from average quartz ratios for each unit ($\delta^{18}O_{melt} \cong \delta^{18}O_{quartz} - 0.4‰$ for high-SiO_2 rhyolites; Bindeman and Valley, 2003; Bindeman, 2008). The calculated $\delta^{18}O_{melt}$ ratios were combined with whole rock isotopic data (Sr–Nd) of OVC rhyolites from Burt et al. (1998), Nairn et al. (2004), and Schmitz and Smith (2004), and whole rock and plagioclase isotopic data (Sr–Pb) of Sas et al. (2021). All isotopic standards were adjusted to the same standard ratios where possible (Supplementary Table A1). Two DMM parental melts and two Torlesse-like metasedimentary assimilants were used for modelling. The DMM parental melts are: (1) a relatively primitive composition represented by a Havre Trough basalt sample (VUW158/4) from the Western Ngatoro Basin, which has been negligibly modified via subduction processes (Gamble et al., 1993, 1996; Macpherson et al., 1998), and (2) a Rumble IV basalt sample (VUW 162/1) from the Eastern Ngatoro Basin, which has been slightly contaminated by a fluid-dominant subduction flux (Gamble et al., 1993, 1996; Macpherson et al., 1998). These off-shore basalts were selected as available O-Sr-Nd-Pb analyses of TVZ basalts indicate crust and/or rhyolite contamination, including at the OVC (e.g., Rotokawau basalt, $\delta^{18}O = 6.0‰$ adjusted; Supplementary Table A1) (Brown et al., 1998). Sample locations of the basaltic endmembers relative to the OVC are shown in the inset map in Fig. 1. The crustal assimilant compositions are: (1) a Torlesse Kaweka member representative composition of Price et al. (2015), with $\delta^{18}O$ ratios from Macpherson et al. (1998), and (2) a Torlesse-like southern TVZ metasedimentary xenolith with enriched Pb isotopes, with compositions from Price et al. (2012, 2015) and average $\delta^{18}O$ ratios from Blattner and Reid (1982). Additional TVZ crustal contaminants (i.e., southern TVZ metaigneous xenoliths, Waipapa metasediments) and parental melts (i.e., OVC basalts) were considered during modelling and are shown along with modelling results. Compositions used for modelling are listed in Supplementary Table A2 and modelling results of $\delta^{18}O$ versus radiogenic isotopes (Sr-Nd-Pb) are shown in Fig. 6.

Modelling results using $\delta^{18}O$ ratios indicate ≥25% assimilation of Torlesse-like metasedimentary crust by a DMM source with minor and variable amounts of subduction flux over the lifespan of the magmatic system might explain the source of the erupted magmas (Fig. 6). Modelling results also demonstrate that (1) OVC basalts do not represent ideal parental melts as their Sr–Nd radiogenic isotope compositions are comparable to those of rhyolites, and (2) that other potential crustal contaminants would not reproduce the isotopic trends observed at the OVC isotopic compositions (i.e., mid-upper crust Waipapa metasediments, Pb isotopic ratios too low; lower crust metaigneous xenoliths found in southern TVZ andesites, Nd isotopic ratios too high; Price et al., 2012) (Fig. 6).

Late-stage crustal contaminants were also considered. Specifically, although $\delta^{18}O$ variability of the rhyolite units is largely within error (0.5‰, 2σ; Fig. 5), the potential impacts of rhyolite assimilation of hydrothermally altered roof materials were assessed based on the presence of the Haparangi outlier quartz (6.7‰) and the lower average whole rock ratios of the other two extra-caldera units, Kakapiko (6.9‰) and Round Hill (7.1‰) (Supplementary Table A1). Assimilation was modelled as both AFC (Supplementary Fig. A5) and simple mixing (Fig. 6; Supplementary Fig. A5) between a representative OVC rhyolite endmember (Rotoiti, $\delta^{18}O = 7.3‰$; Supplementary Table A1) and a co-magmatic, hydrothermally altered, granitoid lithic found in Kaharoa ($2.8 \pm 1.1‰$; Brown et al., 1998) (Supplementary Table A2). Compositionally, the granitoid lithic is nearly identical to the rhyolites (Fig. 2; Supplementary Table A2), therefore AFC (at $F < 0.5$ and $r = 0.3$; McCulloch et al., 1994; Price et al., 2012; Sas et al., 2021) and mixing have little impacts on rhyolite compositions (Supplementary Fig. A5). Isotopically, modelling demonstrates two points. First, due to the moderate $\delta^{18}O$ ratios and nearly identical Sr-Nd-Pb ratios (relative to rhyolites), <5% assimilation of hydrothermally altered material is undetectable in caldera and intra-caldera rhyolites. Second, incorporation of ~7–10% of hydrothermally altered material could produce the lower ratios observed in extra-caldera units (Fig. 6). Thus, it is possible that extra-caldera units (i.e., Kakapiko, Haparangi, Round Hill) assimilated altered roof material, albeit physical evidence for such substantial

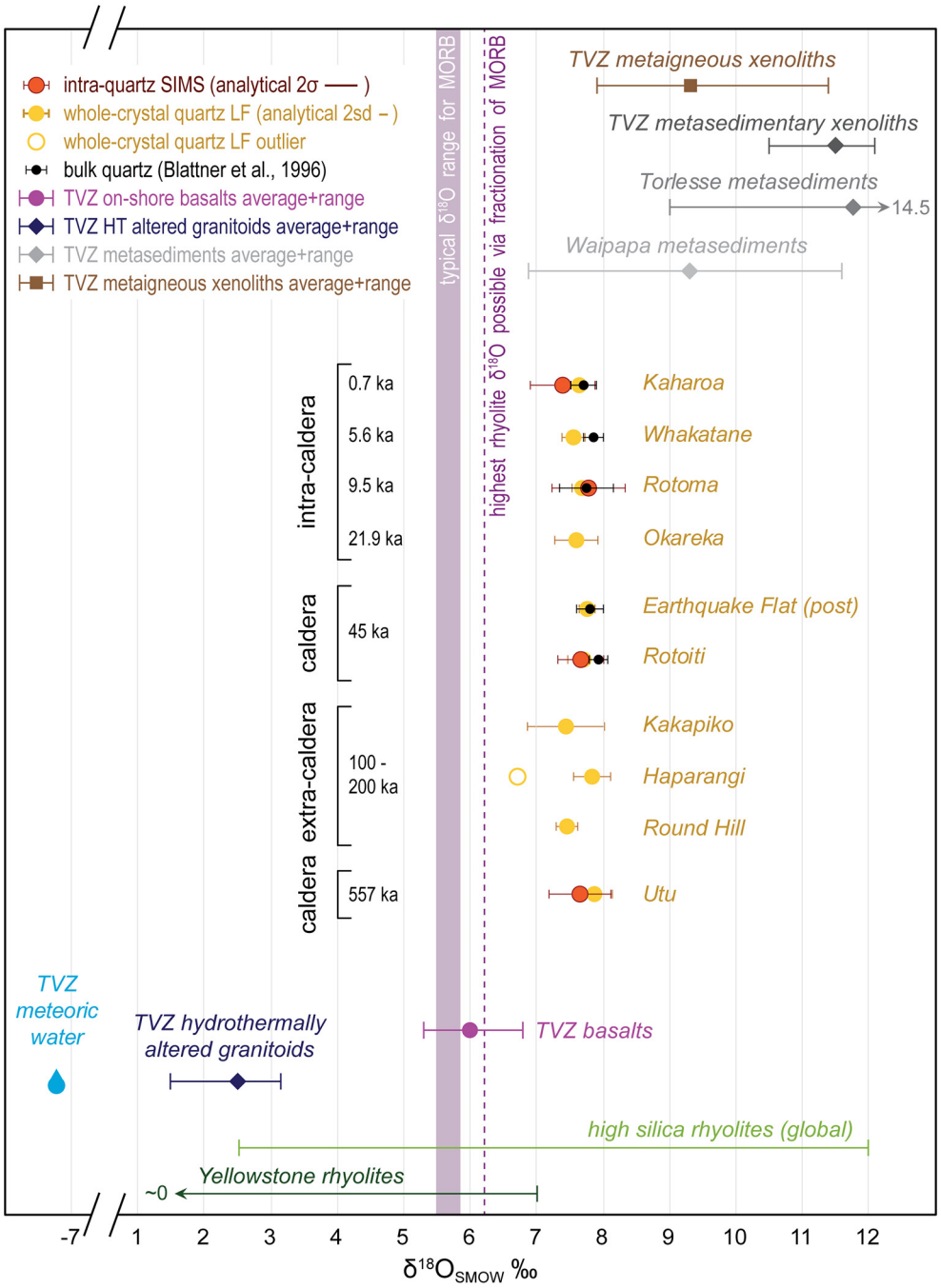

Fig. 5. $\delta^{18}O$ ratios of OVC rhyolites plotted with $\delta^{18}O$ ratio ranges for TVZ on-shore basalts, metasediments, hydrothermally altered granitoids, and meteoric water, as well as typical MOR basalt (MORB) ratios and global high silica rhyolite ratios. OVC rhyolite $\delta^{18}O$ ratios include means of intra-crystal SIMS analyses (large red circles), whole-crystal LF analyses (large yellow circles), and bulk (multi-crystal) quartz analyses (small black circles; Blattner et al., 1996). Ratios of typical MORB, MORB-derived rhyolitic melts, high silica rhyolites, and Yellowstone rhyolites are from Bindeman (2008). Range of TVZ rhyolite-hosted, hydrothermally altered granitoid lithics are from Brown et al. (1998). Ranges of TVZ basalts, Torlesse and Waipapa metasediments, and southern TVZ metasedimentary xenoliths are from Blattner and Reid (1982) and McCulloch et al. (1994). All whole rock $\delta^{18}O$ ratios from literature have been corrected to NBS28 = 9.29‰ (Kusakabe and Matsuhisa, 2008), with original ratios and corrected ratios listed in Supplementary Table A1. Meteoric water data are from Taylor et al. (1977).

incorporation of hydrothermally altered material is absent in the TVZ (Brown et al., 1998). Alternatively, the trio may have experienced some degree of hydrothermal alteration similar to the granitoid lithic. Specifically, it is suggested that the extra-caldera units could potentially represent remobilized plutons based on their high crystallinity (20–40%), petrological and geochemical similarities, and proximity to Earthquake Flat (Sas et al., 2021), which Molloy et al. (2008) suggest was a rejuvenated, partially-crystalline, rhyolitic pluton.

Overall, the models are consistent with AFC and radiogenic modelling results of OVC rhyolites based on whole rock and plagioclase (Sas et al., 2021), as well as recent studies that call on high percentages (20–30% based on radiogenic isotopes; Fig. 6) of DMM partial melting for TVZ intra-caldera basalt petrogenesis (Waight et al., 2017; Zellmer et al., 2020; Barker et al., 2020). Large volumes of melt in the upper mantle (≤12%; Stern and Benson, 2011), lower crust (≤2%; Heise et al., 2010), and middle crust (≤ 4%; Harrison and White, 2006) have also

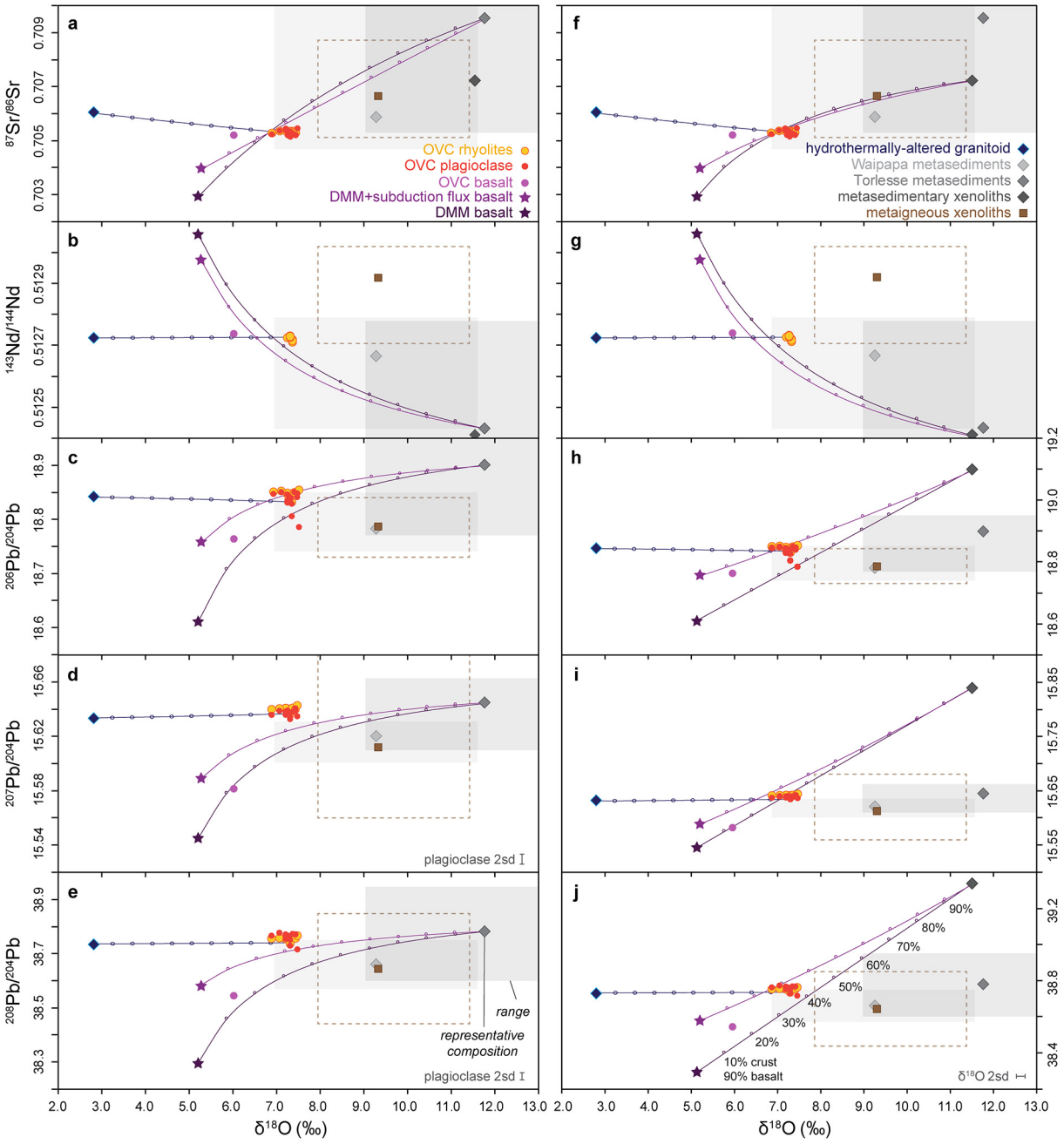

Fig. 6. Simple isotopic mixing models using off-shore TVZ DMM basalts (stars) as parents and Torlesse-like metasediments (dark grey diamonds) as assimilants. All compositions used for modelling are listed in Supplementary Table A2. Assimilant compositions used for modelling consist of the Torlesse Kaweka representative composition in (a–e) and a metasedimentary xenolith composition in (f–i) (Price et al., 2012, 2015). Representative compositions of other potential isotopic contaminants (Waipapa metasediments, light grey diamond; metaigneous xenoliths, brown square) and parents (OVC basalt, purple circle) are included for reference and are also listed in Supplementary Table A2. Square regions represent isotopic ranges for the Torlesse metasediments (dark grey, shaded), Waipapa metasediments (light grey, shaded), and metaigneous xenoliths from the southern TVZ that are thought to be representative of the lower crust (brown, dashed outline). Isotopic data for the metasedimentary xenoliths are limited and therefore no range is available (Supplementary Table A2; Price et al., 2012, 2015). Also included are simple isotopic mixing lines between a hydrothermally altered OVC granitoid (dark blue diamond; Brown et al., 1998) and OVC rhyolites, with compositional mixing and AFC models shown in Supplementary Fig. A5. All isotopic ratios (O-Sr-Nd-Pb) have been adjusted to a common standard ratio where possible (e.g., all $\delta^{18}O$ ratios have been corrected to NBS29; Kusakabe and Matsuhisa, 2008). The original reported isotopic ratios, the corrected isotopic ratios, and the respective references for each unit are listed in Supplementary Table A1. For OVC rhyolites, only Pb isotopic data of Sas et al. (2021) were used (whole rock and plagioclase) as Pb ratios from previous studies could not be corrected (Supplementary Table A1). The LF error of $\delta^{18}O$ ratios (±0.1‰, 2sd; Table 3) is included on the bottom right of panel j. Errors of whole rock Sr-Nd-Pb isotopic ratios (Supplementary Table A1) and plagioclase Sr and $^{206}Pb/^{204}Pb$ isotopic ratios (Sas et al., 2021) are smaller than their respective data symbols, thus they are not included. Where plagioclase errors (2sd) are larger than the respective data symbols, errors have been included on the bottom left of the panel. There are no plagioclase Nd isotopes, and whole Nd isotopic ratios are only available for Kaharoa, Earthquake Flat, and Rotoiti (Supplementary Table A1), therefore the isotopic range of OVC rhyolites in panels b and g is narrower.

been previously suggested by geophysical studies at the OVC. Fig. 7 provides a simplified schematic model for rhyolite petrogenesis at the OVC based on these geophysical data, our models, and previously published petrogenic models (e.g., Smith et al., 2005; Molloy et al., 2008; Shane et al., 2008a, 2008b; and others). This conceptual model shows that the zone of metasediment assimilation is largely restricted to the roots

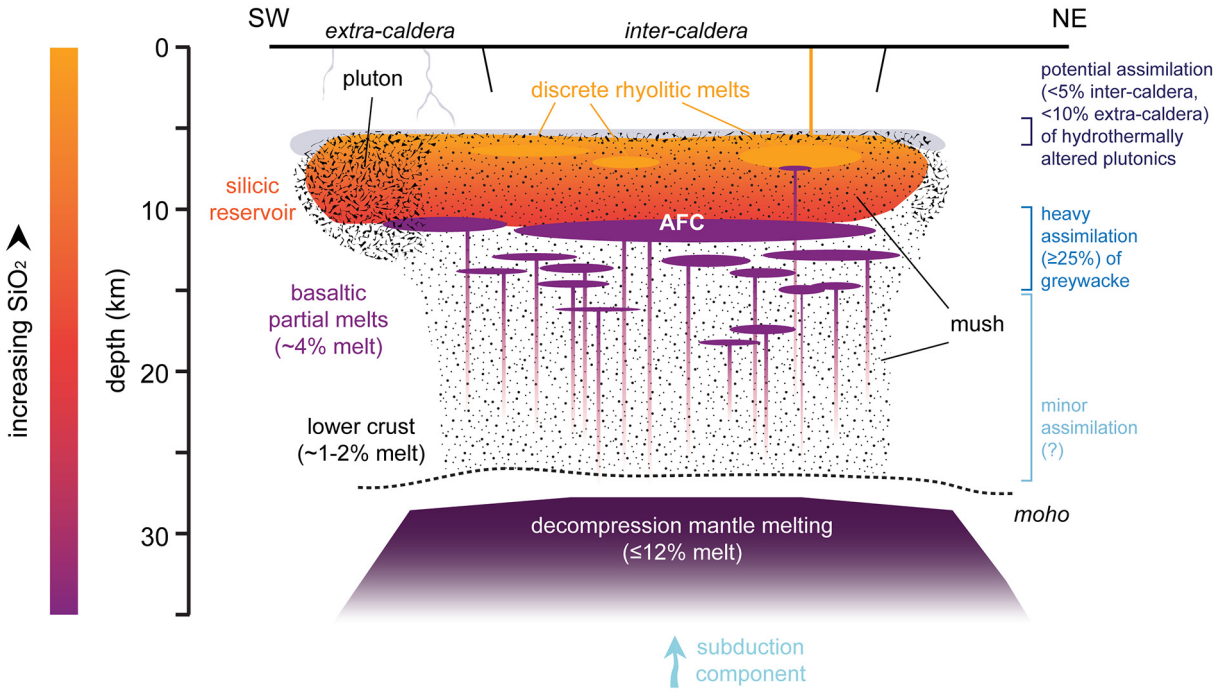

Fig. 7. Schematic model for magma genesis at the OVC based on geophysical and petrological models, as well as AFC and mixing isotopic models (Sas et al., 2021; this study). The mantle beneath the OVC melts as a result of decompression and variable subduction flux, with the upper mantle containing as much as ~12% melt (Stern and Benson, 2011). The middle to lower crust beneath the OVC is then heavily intruded by mantle-derived basalt and contains as much as ~1–2% melt (Harrison and White, 2006). The basaltic melts stall at approximately 10–15 km depth, where they assimilate Torlesse-like metasedimentary crustal materials and fractionate (Sas et al., 2021; this study). Melt content at ~10 km depth is thought to be as high as 4% (Heise et al., 2010). Periodic basaltic melts penetrate the silicic reservoir and provide heat and volatiles to isolated silicic melt pods, consequently triggering movement of rhyolitic melts and eruption largely via contribution of heat and volatiles. Assimilation of hydrothermally altered materials, if present, is more dominant in extra-caldera settings, where the reservoir is mostly crystalline.

of the reservoir where parental magmas reside, and occurs prior to the segregation of fractionated melt based on the largely homogenous stable (this study) and radiogenic (Sas et al., 2021) isotopic ratios, whereas any potential impact of hydrothermal alteration is restricted to the uppermost reservoir and is more prominent in extra-caldera settings.

5.3. Quartz $\delta^{18}O$ records in caldera systems

The observed isotopic homogeneity at the OVC will herein be discussed in context to other major global silicic centres in several tectono-magmatic settings. Changes in oxygen isotopic ratios of magmas, which have been ascribed to open system processes, have been recognized in pre-, *syn*-, and post- caldera-forming events at several silicic volcanic centers of various tectonic settings. Commonly, a decrease in $\delta^{18}O$ ratios at these centers is attributed to mafic influx and/or melting and incorporation of low-$\delta^{18}O$, hydrothermally altered material. For instance, quartz and other minerals erupted from the intra-plate Yellowstone and Snake River Plain caldera centers exhibit significant $\delta^{18}O$ ratio diversity. Specifically, crystals in deposits from three caldera eruptions at Yellowstone (~2 Ma, 1.3 Ma, and 0.64 Ma with ~2500 km^3, ~300 km^3, and ~1000 km^3, respectively) exhibit notable within-unit heterogeneity (quartz $\delta^{18}O$ ratios variability of ~0.5–1.8‰) (Hildreth et al., 1984; Bindeman and Valley, 2000, 2001). The differences between quartz crystals from the three Yellowstone caldera deposits are even larger (up to ~2.6‰). Furthermore, quartz crystals from post-2 Ma and post-0.64 Ma intra-caldera lavas reflect significant drops in $\delta^{18}O$ ratios relative to their precursory caldera events (as much as ~6‰, Fig. 8a). Quartz crystals from extra-caldera lavas, in contrast, have maintained $\delta^{18}O$ ratios that overlap with the 2 Ma caldera event (Hildreth et al., 1984; Bindeman and Valley, 2000, 2001). The authors note that the observed drops in $\delta^{18}O$ ratios are too large to be explained by MOR basalt-like parental melts, and instead require voluminous crustal assimilation of hydrothermally altered rock following evacuation of the silicic reservoir. Older rhyolite calderas from the Snake River Plain, namely Bruneau-Jarbidge, 12.7–8.1 Ma (Boroughs et al., 2005; Bindeman and Simakin, 2014), Picabo, 10.5–6.6 Ma (Drew et al., 2013), and Heise, 6.6–3.9 Ma (Bindeman et al., 2007; Watts et al., 2011), all have similar shifts in $\delta^{18}O$ ratios associated with caldera collapse with similar proposed origins. Specifically, within-unit variations of quartz $\delta^{18}O$ ratios at these centers reach 1.5‰, and between-unit variations are as large as 4‰.

Drops in $\delta^{18}O$ have also been noted in a subduction setting in Sumatra (Indonesia), which is situated on thick continental crust (>35 km; Sakaguchi et al., 2006). An intra-crystal investigation of the youngest caldera-forming event at Toba volcano (Young Toba Tuff, ~2800 km^3, 75 ka) also calls on incorporation of hydrothermally altered crustal material (Budd et al., 2017). The authors noted overall lower (relative to the core) $\delta^{18}O$ ratios in quartz rims, with core-to-rim variations as large as 1.8‰, and several per mil inter-crystal variation (Fig. 8b).

Similar fluctuations in $\delta^{18}O$ ratios are also observed at caldera centers in the continental extensional setting of the Basin and Range province (western United States). Quartz and other minerals in deposits from voluminous caldera eruptions (>900 km^3, 12.8–11.45 Ma) at the Southwestern Nevada Volcanic Field show within-unit $\delta^{18}O$ ratio variability of 0.6–1.2‰ and between-unit variability of ~3.0‰ (Bindeman and Valley, 2003). The authors interpreted the isotopic variations to involve rapid magma generation through mafic influx, and subsequent assimilation of isotopically varied (due to hydrothermal alteration) crustal rocks.

In contrast to these systems, the OVC is situated in an actively rifting arc (~12 mm/yr at the OVC; Wallace et al., 2004) with thin continental crust (~25 km; Bannister et al., 2004), where the modern subduction tectonic regime began ~16 Ma (Wilson and Rowland, 2016). Eruption frequency at the OVC is high (millennial timescales), the magmatic

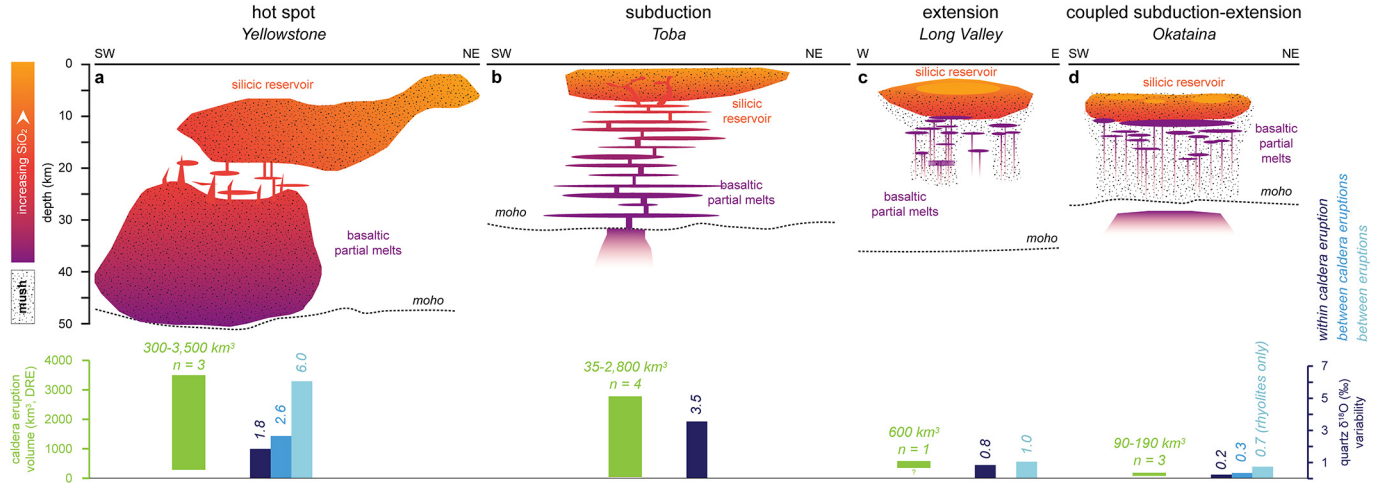

Fig. 8. Simplified illustration comparing rhyolite magma genesis models and silicic reservoir dynamics at caldera-forming centers of different tectonic settings, as well as their respective known number of caldera eruptions (n), estimated DRE volumes (km^3), and variability noted in quartz $\delta^{18}O$ isotopic ratios (‰). (a) The Yellowstone caldera, western United States, is situated in thick continental crust and is associated with hot spot magmatism (after Huang et al., 2015; ratios and volumes from Hildreth et al., 1984 and Bindeman and Valley, 2000, 2001). (b) The Toba caldera, Indonesia, is situated in a subduction setting (modified after Jaxybulatov et al., 2014; ratios and volumes from Budd et al., 2017). (c) The Long Valley caldera is situated in the Basin and Range extension province in western United States (after Hildreth and Wilson, 2007; ratios and volumes from Bindeman and Valley, 2002 and Hildreth, 2004). (d) The OVC, North Island, Aotearoa New Zealand, is situated in a coupled subduction-extension setting where the continental crust is thin (simplified from Fig. 7; $\delta^{18}O$ ratios from this study and volumes from Cole et al., 2014).

system is relatively young (~0.6 Ma; Leonard et al., 2010), and eruption volume magnitudes are comparatively lower (90–190 km^3 per caldera collapse event, Table 1; Nairn, 2002; Smith et al., 2005; Shane et al., 2008b; Deering et al., 2011). This high frequency of volcanic activity, along with homogeneous isotopic compositions, indicate a steady influx of mantle material into the system and constant mechanisms of crustal assimilation. Although $\delta^{18}O$ ratio differences were noted in lava external to the caldera and suggest that assimilation of hydrothermally altered material and/or hydrothermal alteration is plausible, they are uncommon (i.e., Haparangi) or subtle (<1‰) and lie within the range of other rhyolites (i.e., Kakapiko, Round Hill), which, in addition to the strikingly similar compositions of hydrothermally altered material and rhyolites, make such assimilation challenging to confirm (Fig. 5, Fig. 6, Supplementary Fig. A5).

The mass flux equilibrium observed at the OVC differs from the other caldera systems discussed above (Fig. 8) but does resemble those of smaller volume (≤600 km^3) caldera systems in extensional setting, such as the Long Valley caldera. The Long Valley caldera is of similar age (0.76–0.04 Ma; Bindeman and Valley, 2002) and is situated in an extensional setting, albeit intra-plate, in the western margin of the ~17 Ma Basin and Range extension province (western United States; Zoback et al., 1981). Although historical extension rates at the Long Valley caldera have varied significantly due to resurgence fluctuations (e.g., ≤70 mm/yr; Hill, 2006), extension rates 60 km SE of the caldera in Owens Valley are similar to extension rates at the OVC (~10 mm/yr; Dixon et al., 1995). Notably, the Long Valley caldera exhibits similar uniformity in $\delta^{18}O$ ratios to those observed at the OVC (Fig. 8c). Specifically, the majority of quartz erupted in the Bishop Tuff event (~600 km^3, 760 ka) have homogeneous ratios that indicate significant (20–30%) crustal assimilation (Bindeman and Valley, 2002; Hildreth, 2004). Unlike at the OVC, however, average pre-caldera lavas (~0.1–1.1 Ma prior) have higher (by ~1‰) and more variable quartz $\delta^{18}O$ ratios than the Bishop Tuff, indicating homogenization of the magmatic storage system prior to the climactic caldera-forming eruption (Bindeman and Valley, 2002). Hildreth and Wilson (2007) also demonstrated that the rhyolitic melts of the Bishop Tuff can be correlated via fractional crystallization, which is not the case for the rhyolitic melts at OVC (e.g., Smith et al., 2006). Similarly, $\delta^{18}O$ fluctuations between the Otowi (1.61 Ma, ~400 km^3) and Tshirege (1.23 Ma, ~250 km^3) Members of the Bandelier Tuff at Valles caldera are <1‰ (Wolff et al., 2002). Like the OVC and Long Valley systems, the intra-plate Valles system is situated in an extensional setting in the Rio Grande Rift (southwestern United States). Albeit both the Valles magmatic system (~2 Ma; Wolff et al., 2002) and the tectonic regime (~26 Ma; Golombek et al., 1983) are older, extension rates in the region over the past 5 Ma are comparable to those of the OVC and Long Valley (~14 mm/yr; Golombek et al., 1983). The similarities of quartz $\delta^{18}O$ ratios between these systems suggests that the extensional setting, as opposed to the subduction setting, has the largest impact on the mass flux dynamics of the OVC magmatic system (Fig. 8d).

6. Conclusions

Despite the resorption textures observed in all quartz crystals from OVC rhyolites, all of the intra-crystal-scale growth zones reveal homogeneous $\delta^{18}O$ ratios (to within ~0.2‰, 2σ). While previous mineral-based studies require nucleation of crystals in discrete, segregated melts within the OVC reservoir, results from this study indicate that the melts from which quartz nucleated were derived from isotopically homogeneous source(s) (to within ~0.5‰, 2σ). The isotopic homogeneity further extends across quartz crystals from rhyolite magmas that differ in age, volume, and vent location. This homogeneity of quartz $\delta^{18}O$ ratios supports the concept of an isotopically homogenized magmatic system below the OVC, with steady contributions from mantle and crust. Simple isotopic mixing models suggest rhyolite genesis involving a DMM basaltic parent with variable subduction flux and significant assimilation (≥25%) of Torlesse-like metasediments. The large degrees of assimilation and the homogeneity of isotopic character require the presence of a voluminous network of mafic melts in the middle to lower crust to provide a vigorous thermal regime, which is supported by seismic and resistivity studies of the region. The isotopic homogeneity observed at the OVC differs from most other rhyolite caldera centers, which commonly exhibit $\delta^{18}O$ fluctuations of ≥1‰ on a crystal-scale and require voluminous incorporation of hydrothermally altered crust, especially following caldera-collapse events. In contrast, quartz from rhyolitic OVC eruptions demonstrates the existence of a relatively buffered isotopic system across the lifespan of the volcano, and no detectable involvement (<5% assimilation) of hydrothermally altered roof rocks in the genesis of intra-caldera and caldera eruption products.

Declaration of Competing Interest

The authors declare that they have no known competing financial interests or personal relationships that could have appeared to influence the work reported in this paper.

Acknowledgements

The authors would also like to thank Ilya Bindeman and Raimundo Brahm for their assistance with some samples, as well as Katy Chamberlain and an anonymous reviewer for their comments, which greatly improved this manuscript. Support for this project comes from the New Zealand Ministry of Business, Innovation, and Employment grant MAUX1507 to GFZ, the University of Auckland to MS, and Monka-sho to HY.

Appendix A. Supplementary data

Supplementary data to this article can be found online at https://doi.org/10.1016/j.jvolgeores.2021.107430.

References

Appleby, S.K., Graham, C.M., Gillespie, M.R., Hinton, R.W., Oliver, G.J.H., EIMF, 2008. A cryptic record of magma mixing in diorites revealed by high-precision SIMS oxygen isotope analysis of zircons. Earth Planet. Sci. Lett. 269, 105–117.

Bachmann, O., Bergantz, G.W., 2004. On the origin of crystal-poor rhyolites: extracted from batholithic crystal mushes. J. Petrol. 45, 1565–1582.

Bachmann, O., Bergantz, G.W., 2008a. Rhyolites and their Source Mushes across Tectonic Settings. J. Petrol. 49, 2277–2285.

Bachmann, O., Bergantz, G.W., 2008b. The magma reservoirs that feed supereruptions. Elements 4, 17–21.

Bachmann, O., Huber, C., 2016. Silicic magma reservoirs in the Earth's crust. Am. Mineral. 101, 2377–2404.

Baertschi, P., 1976. Absolute 18O Content of standard mean ocean water. Earth Planet. Sci. Lett. 31, 341–344.

Bannister, S., Bryan, C.J., Bibby, H.M., 2004. Shear wave velocity variation across the Taupo Volcanic Zone, New Zealand, from receiver function inversion. Geophys. J. Int. 159, 291–310.

Barker, S.J., Rowe, M.C., Wilson, C.J.N., Gamble, J.A., Rooyakkers, S.M., Wysoczanski, R.J., Illsley-Kemp, F., Kenworthy, C.C., 2020. What lies beneath? Reconstructing the primitive magmas fueling voluminous silicic volcanism using olivine-hosted melt inclusions. Geology 48, 504–508.

Bindeman, I., 2008. Oxygen isotopes in mantle and crustal magmas as revealed by single crystal analysis. Rev. Mineral. Geochem. 69, 445–478.

Bindeman, I.N., Simakin, A.G., 2014. Rhyolites—Hard to produce, but easy to recycle and sequester: integrating microgeochemical observations and numerical models. Geosphere 10, 930–957.

Bindeman, I.N., Valley, J.W., 2000. Formation of low-δ18O rhyolites after caldera collapse at Yellowstone, Wyoming, USA. Geology 28, 719–722.

Bindeman, I.N., Valley, J.W., 2001. Low-δ18O rhyolites from yellowstone: magmatic evolution based on analyses of zircons and individual phenocrysts. J. Petrol. 42, 1491–1517.

Bindeman, I.N., Valley, J.W., 2002. Oxygen isotope study of the Long Valley magma system, California: isotope thermometry and convection in large silicic magma bodies. Contrib. Mineral. Petrol. 144, 185–205.

Bindeman, I.N., Valley, J.W., 2003. Rapid generation of both high- and low-δ18O, large-volume silicic magmas at the Timber Mountain/Oasis Valley caldera complex, Nevada. Geol. Soc. Am. Bull. 18.

Bindeman, I.N., Watts, K.E., Schmitt, A.K., Morgan, L.A., Shanks, P.W.C., 2007. Voluminous low δ18O magmas in the late Miocene Heise volcanic field, Idaho: implications for the fate of Yellowstone hotspot calderas. Geology 35, 1019–1022.

Blattner, P.E., Reid, F., 1982. Origin of lavas and ignimbrites of the Taupo Volcanic Zone, New Zealand, in the light of oxygen isotope data. Geochim. Cosmochim. Acta 46, 1417–1429.

Blattner, P.E., Rui-Zhong, H., Graham, I.J., Houston-Eleftheriadis, C., 1996. Temperatures and isotopic evolution of silicic magmas, Taupo Volcanic Zone and Coromandel, New Zealand. N. Z. J. Geol. Geophys. 39, 353–362.

Boroughs, S., Wolff, J., Bonnichsen, B., Godchaux, M., 2005. Large-volume, low-δ18O rhyolites of the Central Snake River Plain, Idaho, USA. Geology 33, 821–824.

Brown, S.J.A., Burt, R.M., Cole, J.W., Krippner, S.J.P., Price, R.C., Cartwright, I., 1998. Plutonic lithics in ignimbrites of Taupo Volcanic Zone, New Zealand; sources and conditions of crystallisation. Chem. Geol. 148, 21–41.

Budd, D.A., Troll, V.R., Deegan, F.M., Jolis, E.M., Smith, V.C., Whitehouse, M.J., Harris, C., Freda, C., Hilton, D.R., Halldórsson, S.A., Bindeman, I.N., 2017. Magma reservoir dynamics at Toba caldera, Indonesia, recorded by oxygen isotope zoning in quartz. Sci. Rep. 7, 40624.

Burt, R.M., Brown, S.J.A., Cole, J.W., Shelley, D., Waight, T.E., 1998. Glass-bearing plutonic fragments from ignimbrites of the Okataina caldera complex, Taupo Volcanic Zone, New Zealand: remnants of a partially molten intrusion associated with preceding eruptions. J. Volcanol. Geotherm. Res. 84, 209–237.

Cole, J.W., Spinks, K.D., Deering, C.D., Nairn, I.A., Leonard, G.S., 2010. Volcanic and structural evolution of the Okataina Volcanic Centre; dominantly silicic volcanism associated with the Taupo Rift, New Zealand. J. Volcanol. Geotherm. Res. 190, 123–135.

Cole, J.W., Deering, C.D., Burt, R.M., Sewell, S., Shane, P.A.R., Matthews, N.E., 2014. Okataina Volcanic Centre, Taupo Volcanic Zone, New Zealand: a review of volcanism and synchronous pluton development in an active, dominantly silicic caldera system. Earth-Sci. Rev. 128, 1–17.

Danišík, M., Shane, P., Schmitt, A.K., Hogg, A., Santos, G.M., Storm, S., Evans, N.J., Keith, Fifield L., Lindsay, J.M., 2012. Re-anchoring the late Pleistocene tephrochronology of New Zealand based on concordant radiocarbon ages and combined 238U/230Th disequilibrium and (U–Th)/He zircon ages. Earth Planet. Sci. Lett. 349–350, 240–250.

Davis, W.J., 1985. Geochemistry and Petrology of the Rotoiti and Earthquake Flat Pyroclastic Deposits. M.S. thesisUniversity of Auckland.

Deering, C.D., Cole, J.W., Vogel, T.A., 2008. A rhyolite compositional continuum governed by lower crustal source conditions in the Taupo Volcanic Zone, New Zealand. J. Petrol. 49, 2245–2276.

Deering, C.D., Gravley, D.M., Vogel, T.A., Cole, J.W., Leonard, G.S., 2010. Origins of cold-wet-oxidizing to hot-dry-reducing rhyolite magma cycles and distribution in the Taupo Volcanic Zone, New Zealand. Contrib. Mineral. Petrol. 160, 609–629.

Deering, C.D., Cole, J.W., Vogel, T.A., 2011. Extraction of crystal-poor rhyolite from a hornblende-bearing intermediate mush: a case study of the caldera-forming Matahina eruption, Okataina volcanic complex. Contrib. Mineral. Petrol. 161, 129–151.

Dixon, T.H., Robaudo, S., Lee, J., Reheis, M.C., 1995. Constraints on present-day Basin and Range deformation from space geodesy. Tectonics 14, 755–772.

Drew, D.L., Bindeman, I.N., Watts, K.E., Schmitt, A.K., Fu, B., McCurry, M., 2013. Crustal-scale recycling in caldera complexes and rift zones along the Yellowstone hotspot track: O and Hf isotopic evidence in diverse zircons from voluminous rhyolites of the Picabo volcanic field, Idaho. Earth Planet. Sci. Lett. 381, 63–77.

Froggatt, P.C., Lowe, D.J., 1990. A review of late Quaternary silicic and some other tephra formations from New Zealand: their stratigraphy, nomenclature, distribution, volume, and age. N. Z. J. Geol. Geophys. 33, 89–109.

Gamble, J.A., Smith, I.E.M., Graham, I.J., Peter, Kokelaar B., Cole, J.W., Houghton, B.F., Wilson, C.J.N., 1990. The petrology, phase relations and tectonic setting of basalts from the Taupo Volcanic Zone, New Zealand and the Kermadec Island Arc - Havre Trough, SW Pacific. J. Volcanol. Geotherm. Res. 43, 253–270.

Gamble, J.A., Smith, I.E.M., McCulloch, M.T., Graham, I.J., Kokelaar, B.P., 1993. The geochemistry and petrogenesis of basalts from the Taupo Volcanic Zone and Kermadec Island Arc, SW Pacific. J. Volcanol. Geotherm. Res. 54, 265–290.

Gamble, J.A., Wright, I.C., Woodhead, J.D., McCulloch, M.T., 1994. Arc and back-arc geochemistry in the southern Kermadec arc-Ngatoro Basin and offshore Taupo Volcanic Zone, SW Pacific. In: Smellie, J.L. (Ed.), Volcanism Assoc. Ext. Consum. Plate Margins Geol. Soc. Spec. Publ. 81, pp. 193–212.

Gamble, J., Woodhead, J., Wright, I., Smith, I., 1996. Basalt and sediment geochemistry and magma petrogenesis in a transect from Oceanic Island arc to rifted continental margin arc: the Kermadec—Hikurangi margin, SW Pacific. J. Petrol. 37, 1523–1546.

Golombek, M.P., McGill, G.E., Brown, L., 1983. Tectonic and geologic evolution of the Espanola Basin, Rio Grande Rift: Structure, rate of extension, and relation to the state of stress in the western United States. Tectonophysics 94, 483–507.

Graham, I.J., Blattner, P., McCulloch, M.T., 1990. Meta-igneous granulite xenoliths from Mount Ruapehu, New Zealand: Fragments of altered oceanic crust? Contrib. Mineral. Petrol. 105, 650–661.

Graham, I.J., Gulson, B.L., Hedenquist, J.W., Mizon, K., 1992. Petrogenesis of Late Cenozoic volcanic rocks from the Taupo Volcanic Zone, New Zealand, in the light of new lead isotope data. Geochim. Cosmochim. Acta 56, 2797–2819.

Harrison, A., White, R.S., 2006. Lithospheric structure of an active backarc basin: the Taupo Volcanic Zone, New Zealand. Geophys. J. Int. 167, 968–990.

Heise, W., Caldwell, T.G., Bibby, H.M., Bennie, S.L., 2010. Three-dimensional electrical resistivity image of magma beneath an active continental rift, Taupo Volcanic Zone, New Zealand. Geophys. Res. Lett. 37, L10301.

Hiess, J., Cole, J.W., Spinks, K.D., 2007. Influence of the crust and crustal structure on the location and composition of high-alumina basalts of the Taupo Volcanic Zone, New Zealand. N. Z. J. Geol. Geophys. 50, 327–342.

Hildreth, W., 2004. Volcanological perspectives on Long Valley, Mammoth Mountain, and Mono Craters: several contiguous but discrete systems. J. Volcanol. Geotherm. Res. 136, 169–198.

Hildreth, W., Wilson, C.J.N., 2007. Compositional Zoning of the Bishop Tuff. J. Petrol. 48, 951–999.

Hildreth, W., Christiansen, R.L., O'Neil, J.R., 1984. Catastrophic isotopic modification of rhyolitic magma at times of caldera subsidence, Yellowstone Plateau Volcanic Field. J. Geophys. Res. 89, 8339–8369.

Hill, D.P., 2006. Unrest in Long Valley Caldera, California, 1978–2004. Geol. Soc. Lond. Spec. Publ. 269, 1–24.

Hogg, A.G., Higham, T.F.G., Lowe, D.J., Palmer, J.G., Reimer, P.J., Newnham, R.M., 2003. A wiggle-match date for Polynesian settlement of New Zealand. Antiquity 77, 116–125.

Huang, H.-H., Lin, F.-C., Schmandt, B., Farrell, J., Smith, R.B., Tsai, V.C., 2015. The Yellowstone magmatic system from the mantle plume to the upper crust. Science 348, 773–776.

Jaxybulatov, K., Shapiro, N.M., Koulakov, I., Mordret, A., Landes, M., Sens-Schonfelder, C., 2014. A large magmatic sill complex beneath the Toba caldera. Science 346, 617–619.

Kawasaki, N., Simon, S.B., Grossman, L., Sakamoto, N., Yurimoto, H., 2018. Crystal growth and disequilibrium distribution of oxygen isotopes in an igneous Ca-Al-rich inclusion from the Allende carbonaceous chondrite. Geochim. Cosmochim. Acta 221, 318–341.

Kobayashi, T., Nairn, I., Smith, V., Shane, P., 2005. Proximal stratigraphy and event sequence of the c. 5600 cal. yr BP Whakatane rhyolite eruption episode from Haroharo volcano, Okataina Volcanic Centre, New Zealand. N. Z. J. Geol. Geophys. 48, 471–490.
Kusakabe, M., Matsuhisa, Y., 2008. Oxygen three-isotope ratios of silicate reference materials determined by direct comparison with VSMOW-oxygen. Geochem. J. 42, 309–317.
Leonard, G.S., Cole, J.W., Nairn, I.A., Self, S., 2002. Basalt triggering of the c. AD 1305 Kaharoa rhyolite eruption, Tarawera volcanic complex, New Zealand. J. Volcanol. Geotherm. Res. 115, 461–486.
Leonard, G.S., Begg, J.G., Wilson, C.J.N., 2010. Geology of the Rotorua Area. Institute of Geological and Nuclear Sciences 1:250,000, Geological Map 5 (1 sheet + 102 p).
Lowe, D.J., Shane, P.A.R., Alloway, B.V., Newnham, R.M., 2008. Fingerprints and age models for widespread New Zealand tephra marker beds erupted since 30,000 years ago: a framework for NZ-INTIMATE. Quat. Sci. Rev. 27, 95–126.
Macpherson, C.G., Gamble, J.A., Mattey, D.P., 1998. Oxygen isotope geochemistry of lavas from an oceanic to continental arc transition, Kermadec–Hikurangi margin, SW Pacific. Earth Planet. Sci. Lett. 160, 609–621.
Matthews, N.E., Huber, C., Pyle, D.M., Smith, V.C., 2012. Timescales of magma recharge and reactivation of large silicic systems from Ti diffusion in quartz. J. Petrol. 53, 1385–1416.
McCulloch, M.T., Kyser, T.K., Woodhead, J.D., Kinsley, L., 1994. Pb-Sr-Nd-O isotopic constraints on the origin of rhyolites from the Taupo Volcanic Zone of New Zealand: evidence for assimilation followed by fractionation from basalt. Contrib. Mineral. Petrol. 115, 303–312.
Milicich, S.D., Mortimer, N., Villamor, P., Wilson, C.J.N., Sagar, M.W., Ireland, T.R., 2021. The Mesozoic terrane boundary beneath the Taupo Volcanic Zone, New Zealand, and potential controls on geothermal system characteristics. N. Z. J. Geol. Geophys. 64, 518–529.
Molloy, C., Shane, P., Nairn, I., 2008. Pre-eruption thermal rejuvenation and stirring of a partly crystalline rhyolite pluton revealed by the earthquake flat pyroclastics deposits, New Zealand. J. Geol. Soc. 165, 435–447.
Nairn, I.A., 2002. Geology of the Okataina Volcanic Centre.
Nairn, I.A., Kohn, B.P., 1973. Relation of the Earthquake Flat Breccia to the Rotoiti Breccia, central North Island, New Zealand. N. Z. J. Geol. Geophys. 16, 269–279.
Nairn, I.A., Shane, P.R., Cole, J.W., Leonard, G.J., Self, S., Pearson, N., 2004. Rhyolite magma processes of the ~AD 1315 Kaharoa eruption episode, Tarawera volcano, New Zealand. J. Volcanol. Geotherm. Res. 131, 265–294.
Price, R.C., Gamble, J.A., Smith, I.E.M., Maas, R., Waight, T., Stewart, R.B., Woodhead, J., 2012. The anatomy of an Andesite Volcano: a time–stratigraphic study of andesite petrogenesis and crustal evolution at Ruapehu Volcano, New Zealand. J. Petrol. 53, 2139–2189.
Price, R., Mortimer, N., Smith, I., Maas, R., 2015. Whole-rock geochemical reference data for Torlesse and Waipapa terranes, North Island, New Zealand. N. Z. J. Geol. Geophys. 58, 213–228.
Reid, F., 1983. Origin of the rhyolitic rocks of the Taupo Volcanic Zone, New Zealand. J. Volcanol. Geotherm. Res. 15, 315–338.
Rubin, A.E., Cooper, K.M., Till, C.B., Kent, A.J., Costa, F., Bose, M., Gravley, D., Deering, C., Cole, J., 2017. Rapid cooling and cold storage in a silicic magma reservoir recorded in individual crystals. Science 356, 1154–1156.
Sahetapy-Engel, S., Self, S., Carey, R.J., Nairn, I.A., 2014. Deposition and generation of multiple widespread fall units from the c. AD 1314 Kaharoa rhyolitic eruption, Tarawera, New Zealand. Bull. Volcanol. 76, 836.
Sakaguchi, K., Gilbert, H., Zandt, G., 2006. Converted wave imaging of the Toba Caldera, Indonesia. Geophys. Res. Lett. 33, L20305.
Sas, M., Kawasaki, N., Sakamoto, N., Shane, P., Zellmer, G.F., Kent, A.J.R., Yurimoto, H., 2019. The ion microprobe as a tool for obtaining strontium isotopes in magmatic plagioclase: a case study at Okataina Volcanic Centre, New Zealand. Chem. Geol. 513, 153–166.
Sas, M., Shane, P., Kuritani, T., Zellmer, G.F., Kent, A.J.R., Nakagawa, M., 2021. Mush, melts and metasediments: a history of rhyolites from Okataina Volcanic Centre, New Zealand, as captured in plagioclase. J. Petrol. 62.
Schmitz, M.D., Smith, I.E.M., 2004. The petrology of the rotoiti eruption Sequence, Taupo Volcanic Zone: an example of fractionation and mixing in a rhyolitic system. J. Petrol. 45, 2045–2066.
Seebeck, H., Nicol, A., Stern, T.A., Bibby, H.M., Stagpoole, V., 2010. Fault controls on the geometry and location of the Okataina Caldera, Taupo Volcanic Zone, New Zealand. J. Volcanol. Geotherm. Res. 190, 136–151.
Shane, P.A.R., 2015. Contrasting plagioclase textures and geochemistry in response to magma dynamics in an intra-caldera rhyolite system, Okataina volcano. J. Volcanol. Geotherm. Res. 297, 1–10.
Shane, P.A.R., Smith, V.C., 2013. Using amphibole crystals to reconstruct magma storage temperatures and pressures for the post-caldera collapse volcanism at Okataina volcano. Lithos 156–159, 159–170.
Shane, P.A.R., Nairn, I.A., Smith, V.C., 2005. Magma mingling in the ~50 ka Rotoiti eruption from Okataina Volcanic Centre: implications for geochemical diversity and chronology of large volume rhyolites. J. Volcanol. Geotherm. Res. 139, 295–313.
Shane, P.A.R., Nairn, I.A., Smith, V.C., Darragh, M., Beggs, K., Cole, J.W., 2008a. Silicic recharge of multiple rhyolite magmas by basaltic intrusion during the 22.6 ka Okareka Eruption Episode, New Zealand. Lithos 103, 527–549.
Shane, P.A.R., Smith, V.C., Nairn, I.A., 2008b. Millennial timescale resolution of rhyolite magma recharge at Tarawera volcano: insights from quartz chemistry and melt inclusions. Contrib. Mineral. Petrol. 156, 397–411.
Shane, P., Storm, S., Schmitt, A.K., Lindsay, J.M., 2012. Timing and conditions of formation of granitoid clasts erupted in recent pyroclastic deposits from Tarawera Volcano (New Zealand). Lithos 140–141, 1–10.
Sharp, Z.D., 1990. A laser-based microanalytical method for the in situ determination of oxygen isotope ratios of silicates and oxides. Geochim. Cosmochim. Acta 54, 1353–1357.
Smith, V.C., Shane, P.A.R., Nairn, I.A., 2005. Trends in rhyolite geochemistry, mineralogy, and magma storage during the last 50 kyr at Okataina and Taupo volcanic centres, Taupo Volcanic Zone, New Zealand. J. Volcanol. Geotherm. Res. 148, 372–406.
Smith, V.C., Shane, P.A.R., Nairn, I.A., Williams, C.M., 2006. Geochemistry and magmatic properties of eruption episodes from Haroharo linear vent zone, Okataina Volcanic Centre, New Zealand during the last 10 kyr. Bull. Volcanol. 69, 57–88.
Smith, V.C., Shane, P.A.R., Nairn, I.A., 2010. Insights into silicic melt generation using plagioclase, quartz and melt inclusions from the caldera-forming Rotoiti eruption, Taupo volcanic zone, New Zealand. Contrib. Mineral. Petrol. 160, 951–971.
Spörli, K.B., 1978. Mesozoic tectonics, North Island, New Zealand. Geol. Soc. Am. Bull. 89, 415–425.
Stern, T., Benson, A., 2011. Wide-angle seismic imaging beneath an andesitic arc: Central North Island, New Zealand. J. Geophys. Res. 116 (B09308), 1–26.
Storm, S., Shane, P.A.R., Schmitt, A.K., Lindsay, J.M., 2011. Contrasting punctuated zircon growth in two syn-erupted rhyolite magmas from Tarawera volcano: Insights to crystal diversity in magmatic systems. Earth Planet. Sci. Lett. 301, 511–520.
Storm, S., Shane, P.A.R., Schmitt, A.K., Lindsay, J.M., 2012. Decoupled crystallization and eruption histories of the rhyolite magmatic system at Tarawera volcano revealed by zircon ages and growth rates. Contrib. Mineral. Petrol. 163, 505–519.
Storm, S., Schmitt, A.K., Shane, P.A.R., Lindsay, J.M., 2014. Zircon trace element chemistry at sub-micrometer resolution for Tarawera volcano, New Zealand, and implications for rhyolite magma evolution. Contrib. Mineral. Petrol. 167, 1000.
Taylor, C.B., Fractions, H.J., Nairn, I.A., 1977. Preliminary measurements of tritium, deuterium and oxygen-18 in lakes and groundwater of volcanic Rotorua region, New Zealand. Inst. Geol. Nucl. Sci. INS-R–227.
Troll, V.R., Deegan, F.M., Jolis, E.M., Harris, C., Chadwick, J.P., Gertisser, R., Schwarzkopf, L.M., Borisova, A.Y., Bindeman, I.N., Sumarti, S., Preece, K., 2013. Magmatic differentiation processes at Merapi Volcano: inclusion petrology and oxygen isotopes. J. Volcanol. Geotherm. Res. 261, 38–49.
Waight, T.E., Troll, V.R., Gamble, J.A., Price, R.C., Chadwick, J.P., 2017. Hf isotope evidence for variable slab input and crustal addition in basalts and andesites of the Taupo Volcanic Zone, New Zealand. Lithos 284–285, 222–236.
Wallace, L.M., Beavan, J., McCaffrey, R., Darby, D., 2004. Subduction zone coupling and tectonic block rotations in the North Island, New Zealand. J. Geophys. Res. 109, B12406.
Wallace, L.M., Reyners, M., Cochran, U., Bannister, S., Barnes, P.M., Berryman, K., Downes, G., Eberhart-Phillips, D., Fagereng, A., Ellis, S., Nicol, A., McCaffrey, R., Beavan, R.J., Henrys, S., Sutherland, R., Barker, D.H.N., Litchfield, N., Townend, J., Robinson, R., Bell, R., Wilson, K., Power, W., 2009. Characterizing the seismogenic zone of a major plate boundary subduction thrust: Hikurangi Margin, New Zealand. Geochem. Geophys. Geosyst. 10, Q10006.
Watts, K.E., Bindeman, I.N., Schmitt, A.K., 2011. Large-volume Rhyolite Genesis in Caldera Complexes of the Snake River Plain: insights from the Kilgore Tuff of the Heise Volcanic Field, Idaho, with Comparison to Yellowstone and Bruneau–Jarbidge Rhyolites. J. Petrol. 52, 857–890.
Wilcock, J., Goff, F., Minarik, W.G., Stix, J., 2013. Magmatic recharge during the formation and resurgence of the Valles Caldera, New Mexico, USA: evidence from quartz compositional zoning and geothermometry. J. Petrol. 54, 635–664.
Wilson, C.J.N., Rowland, J.V., 2016. The volcanic, magmatic and tectonic setting of the Taupo Volcanic Zone, New Zealand, reviewed from a geothermal perspective. Geothermics 59, 168–187.
Wilson, C.J.N., Houghton, B.F., McWilliams, M.O., Landphere, M.A., Weaver, S.D., Briggs, R.M., 1995. Volcanic and structural evolution of Taupo Volcanic Zone, New Zealand: a review. J. Volcanol. Geotherm. Res. 68, 1–28.
Wolff, J.A., Balsley, S.D., Gregory, R.T., 2002. Oxygen isotope disequilibrium between quartz and sanidine from the Bandelier Tuff, New Mexico, consistent with a short residence time of phenocrysts in rhyolitic magma. J. Volcanol. Geotherm. Res. 116, 119–135.
Zellmer, G.F., Kimura, J.-I., Stirling, C.H., Lube, G., Shane, P.A., Iizuka, Y., 2020. Genesis of recent mafic magmatism in the Taupo Volcanic Zone, New Zealand: insights into the birth and death of very large volume rhyolitic systems? J. Petrol. 61, egaa027.
Zoback, M.L., Anderson, R.E., Thompson, G.A., 1981. Cainozoic evolution of the state of stress and style of tectonism of the basin and range province of the Western United States. Philos. Trans. R. Soc. A Math. Phys. Eng. Sci. 300, 407–434.